J. Fluid Mech. (2013), *vol.* 727, *pp.* 612–647.
doi:10.1017/jfm.2013.280

Drops walking on a vibrating bath: towards a hydrodynamic pilot-wave theory

Jan Moláček and John W. M. Bush†

Department of Mathematics, Massachusetts Institute of Technology, 77 Massachusetts Avenue, Cambridge, MA 02139, USA

(Received 7 December 2012; revised 1 April 2013; accepted 24 May 2013; first published online 28 June 2013)

We present the results of a combined experimental and theoretical investigation of droplets walking on a vertically vibrating fluid bath. Several walking states are reported, including pure resonant walkers that bounce with precisely half the driving frequency, limping states, wherein a short contact occurs between two longer ones, and irregular chaotic walking. It is possible for several states to arise for the same parameter combination, including high- and low-energy resonant walking states. The extent of the walking regime is shown to be crucially dependent on the stability of the bouncing states. In order to estimate the resistive forces acting on the drop during impact, we measure the tangential coefficient of restitution of drops impacting a quiescent bath. We then analyse the spatio-temporal evolution of the standing waves created by the drop impact and obtain approximations to their form in the small-drop and long-time limits. By combining theoretical descriptions of the horizontal and vertical drop dynamics and the associated wave field, we develop a theoretical model for the walking drops that allows us to rationalize the limited extent of the walking regimes. The critical requirement for walking is that the drop achieves resonance with its guiding wave field. We also rationalize the observed dependence of the walking speed on system parameters: while the walking speed is generally an increasing function of the driving acceleration, exceptions arise due to possible switching between different vertical bouncing modes. Special focus is given to elucidating the critical role of impact phase on the walking dynamics. The model predictions are shown to compare favourably with previous and new experimental data. Our results form the basis of the first rational hydrodynamic pilot-wave theory.

Key words: drops, Faraday waves, waves/free-surface flows

1. Introduction

A liquid drop placed on a vibrating liquid bath can achieve a vertical bouncing motion by virtue of the sustenance of an air layer between the drop and bath (Walker 1978; Couder *et al.* 2005*a*). For drops within a certain size range, the interplay between the drop and the waves it excites on the liquid surface causes the vertical bouncing state to become unstable to a walking state (Couder *et al.* 2005*b*). The interaction of the walking drops and their guiding wave field leads to a variety of phenomena reminiscent of quantum mechanics, including tunnelling across

† Email address for correspondence: bush@math.mit.edu

a subsurface barrier (Eddi *et al.* 2009), single-particle diffraction in the single- and double-slit geometries (Couder & Fort 2006), quantized orbits (Fort *et al.* 2010) and orbital level splitting (Eddi *et al.* 2012). This hydrodynamic system bears a remarkable similarity to an early model of quantum dynamics, the pilot-wave theory of Louis de Broglie (de Broglie 1987; Bush 2010; Harris *et al.* 2013).

Protière, Boudaoud & Couder (2006) presented a regime diagram of liquid drops bouncing on a liquid bath (specifically, 20 cSt silicone oil), as did Eddi *et al.* (2008) for 50 cSt oil. In Moláček & Bush (2013, henceforth MBI), we have extended their measurements to cover a wider range of drop size and driving frequency, in order to have a firmer experimental basis for building a theoretical model for the drop's vertical dynamics. In MBI, we developed a hierarchy of theoretical models and showed that the experimental results are best matched by describing the interaction as a logarithmic spring, analogously to impacts on rigid substrates (Moláček & Bush 2012). We noted the existence of two distinct modes with the same period and number of jumps per period, which we refer to as 'vibrating' and 'bouncing' modes. In the lower-energy vibrating mode, the contact time of the drop is set by the vibration frequency of the bath; while in the higher-energy bouncing mode, it is set by the drop's characteristic frequency of oscillations. The possible coexistence of these two vertical modes for the same parameter combination will be relevant here.

In order to understand the role of drop size and driving frequency on the bouncing dynamics, a model of both the vertical and horizontal drop motion is required. No satisfactory quantitative model exists to date. Couder *et al.* (2005*b*) introduced a simple model of walking drops that was further developed by Protière *et al.* (2006), both models being based on the approximation that the wave field is sinusoidal and centred on the last impact. The shear drag in the intervening air layer was misidentified as the major force resisting the drop's horizontal motion, an assumption to be corrected here. We also point out the shortcomings of their scaling for the averaged reaction force acting on the drop, $F \sim m\gamma(\tau/T_F)$, where m is drop mass, γ the driving acceleration, τ the contact time and T_F the Faraday period. If the drop is to keep bouncing, the average reaction force must equal the drop weight: $F = mg$. It will be shown here that the horizontal force on the drop increases with driving acceleration, not because of an increasing vertical reaction force, but due to an increase in the magnitude of the standing-wave pattern induced as one approaches the Faraday threshold.

Eddi *et al.* (2011) presented a more detailed model that included the contributions to the wave field from all previous impacts, but the divergence of their wave field approximation at the centre of the impact precludes its suitability for modelling the transition from simple bouncing to walking. While the theoretical models of Couder's group capture certain key features of the walker dynamics, they contain a number of free parameters that can only be eliminated by careful consideration of the impact dynamics. More recently, Shirokoff (2013) treated the wave field created by drop impacts in more detail, but only the most recent impact was considered; moreover, no connection was made between the model's free parameters and the experiments.

The goal of this paper is to develop a theoretical model capable of providing a quantitative rationale for the regime diagrams of the bouncing drops, such as that shown in figure 4. In addition to rationalizing the limited extent of the walking regime, the model should allow us to understand the observed dependence of the walking speed on the bath acceleration. By time averaging over the vertical dynamics described in MBI, we here develop a trajectory equation for the walking drops. Our model predicts the existence of several of the experimentally observed walking states, such

as low- and high-energy resonant walking, limping and chaotic walking. The possible coexistence of these states at the same parameter combination may give rise to a complex mode-switching dynamics.

In § 2 we describe our experimental arrangement and present our data describing the observed dependence of the walking thresholds and speeds on the system parameters. In § 3 we analyse the spatio-temporal evolution of the standing waves created by a drop impact on the liquid bath for peak driving accelerations near the Faraday threshold. In § 4, we consider all the major forces acting on the drop during flight and rebound, and so obtain a consistent model for the drop's horizontal and vertical dynamics. By analysing the model in the limit of short contact time relative to the driving period, we obtain a trajectory equation appropriate for small walking drops. In § 5 we present the model predictions and compare them to the experimental data. Specifically, we examine the role of drop size and driving acceleration on the walking speed, and the role of oil viscosity and driving frequency on the extent of the walking regime. We also highlight the role of the vertical dynamics in setting the boundaries of the walking regime. Some simplifications of the full model are made in order to obtain a relatively simple scaling for the walking speed and insight into the walking thresholds. Future research directions are outlined in § 6.

2. Experiments

In order to extend the datasets reported by Protière *et al.* (2006) and Eddi *et al.* (2011), we measured the walking thresholds and walking speeds of droplets of silicone oil of kinematic viscosity 20 and 50 cSt, for a broad range of drop sizes and driving frequencies. A schematic illustration of the experimental apparatus is shown in figure 1. A liquid drop of undeformed radius R_0 bounces on a bath of the same liquid (figure 2), in our case silicone oil with density $\rho = 949$ kg m^{-3}, surface tension $\sigma = 20.6 \times 10^{-3}$ N m^{-1} and kinematic viscosity $\nu = 20$ cSt, or a more viscous silicone oil with $\rho = 960$ kg m^{-3}, $\sigma = 20.8 \times 10^{-3}$ N m^{-1} and $\nu = 50$ cSt. The bath of depth $h_B \approx 9$ mm is enclosed in a cylindrical container with diameter $D = 76$ mm. The container is shaken vertically, sinusoidally in time, with peak acceleration γ and frequency f, so that the effective gravity in the bath frame of reference is $g + \gamma \sin(2\pi ft)$. The motion of the drop was observed using a high-speed camera synchronized with the shaker. The camera resolution is 86 pixel mm^{-1}, and the distance of the drop from the camera was controlled with approximately 1 % error by keeping the drop in focus, giving a total error in our drop radius measurement of less than 0.01 mm. The drops were created by dipping a needle in the bath then quickly retracting it (Protière *et al.* 2006). The drop's initial conditions play little role in its subsequent dynamics, provided coalescence is avoided. However, a certain amount of hysteresis may arise as the various thresholds are crossed.

The notation adopted in this paper, together with the range of values of the various physical variables, are shown in table 1. Following Gilet & Bush (2009), we adopt the (m, n) notation to distinguish between different bouncing modes. In the (m, n) mode, the drop's vertical motion has a period of m driving periods, during which the drop contacts the bath n times. Multiple bouncing modes corresponding to the same (m, n) number may exist, and we shall differentiate them according to their mean energy using a superscript, following MBI. In particular, $(m, n)^1$ will denote the lower-energy 'vibrating' mode, in which the drop spends a large fraction of its bouncing period in contact with the bath, while $(m, n)^2$ will denote the higher-energy 'bouncing' mode, in

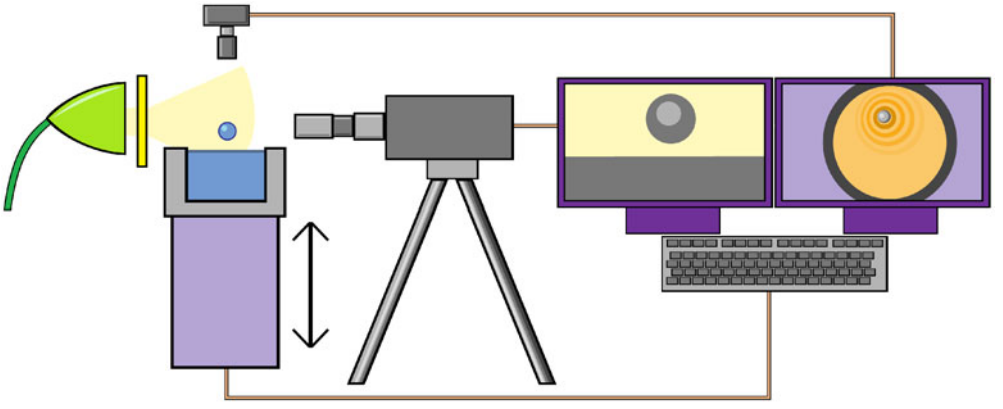

FIGURE 1. (Colour online) The experimental set-up. A liquid drop bounces on a vibrating liquid bath enclosed in a circular container. The drop is illuminated by a light-emitting diode lamp, its vertical motion recorded on a high-speed camera and its horizontal motion recorded on a top-view camera. Both cameras are synchronized with the shaker.

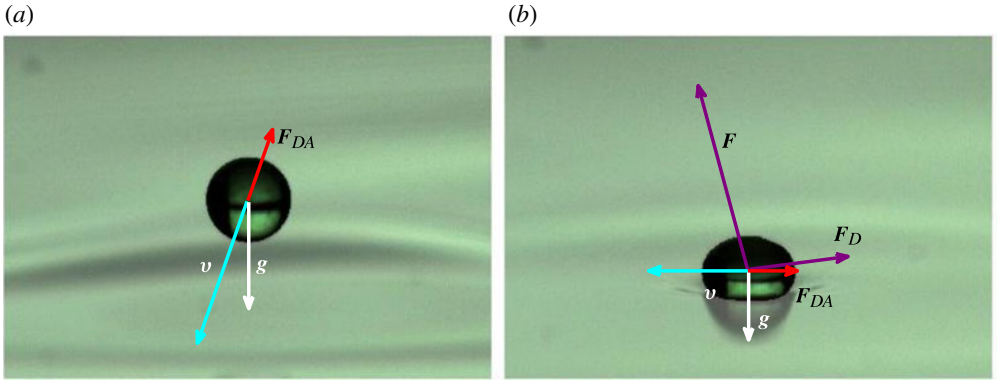

FIGURE 2. (Colour online) A droplet of radius $R_0 = 0.38$ mm (a) in flight and (b) during contact with the bath. During flight, its motion is accelerated by the gravitational force $\boldsymbol{g}$ and resisted by the air drag $\boldsymbol{F}_{DA}$ that opposes its motion $\boldsymbol{v}$. During contact, two additional forces act on the drop; the reaction force $\boldsymbol{F}$ normal to the bath surface and the momentum drag force $\boldsymbol{F}_D$ tangential to the surface and proportional to the tangential component of $\boldsymbol{v}$.

which the contact is relatively short. The $(2, 1)^1$, $(2, 1)^2$ and $(2, 2)$ walking modes are shown in figure 3, together with more complex behaviours observed in walking drops.

2.1. *Walking thresholds and speeds*

Each impact of the drop on the vibrating liquid bath creates a transient wave that propagates outwards from the centre of impact, leaving in its wake a standing Faraday wave pattern that decays exponentially with both time and distance from the impact centre (Eddi *et al.* 2011). As the driving is increased, the temporal decay rate of the standing-wave pattern decreases and the total amplitude of the surface deformation increases, being the sum of the standing waves generated by all previous impacts. When the drop is in the $(2, 1)$ bouncing mode, it lands on the bath when the

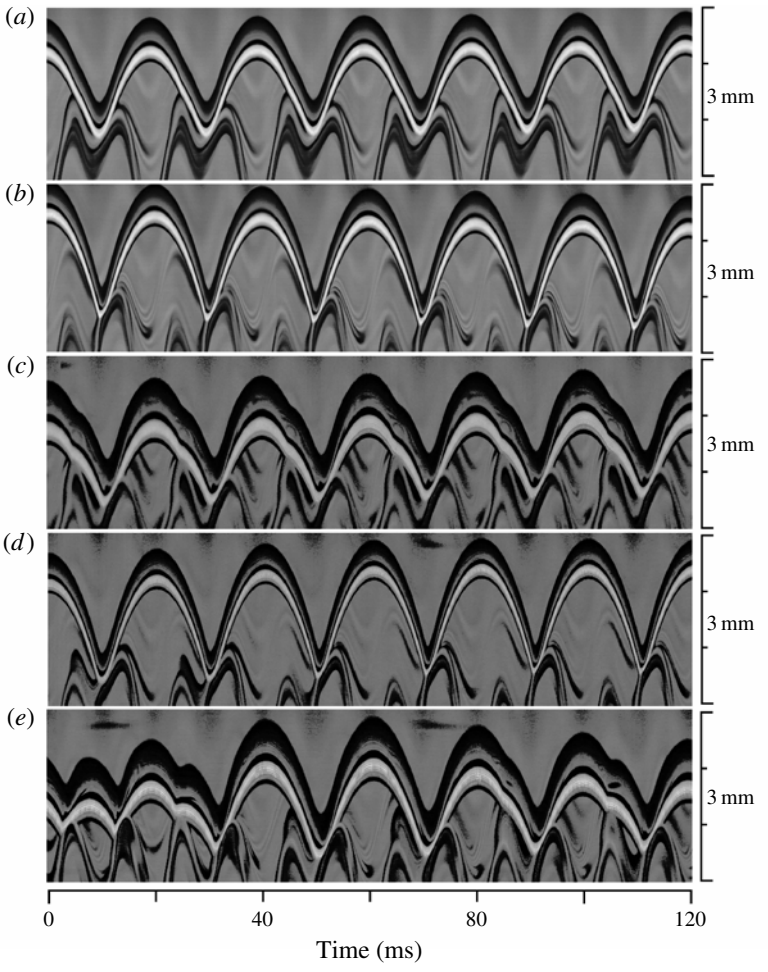

FIGURE 3. Examples of the vertical motion of 50 cSt silicone oil drops walking on a liquid bath vibrating with frequency 50 Hz. These are, in order of increasing complexity: (*a*) the $(2, 1)^1$ mode, $R_0 = 0.39$ mm, $\Gamma = 3.6$; (*b*) the $(2, 1)^2$ mode, $R_0 = 0.39$ mm, $\Gamma = 4.1$; (*c*) the $(2, 2)$ limping mode, $R_0 = 0.57$ mm, $\Gamma = 4.0$; (*d*) switching between the $(2, 1)^1$ and $(2, 1)^2$ modes that arises roughly every 20 forcing periods, $R_0 = 0.35$ mm, $\Gamma = 4.0$; and (*e*) chaotic bouncing, $R_0 = 0.57$ mm, $\Gamma = 4.0$. Here R_0 is the drop radius and $\Gamma = \gamma/g$ is the dimensionless driving acceleration. The images were obtained by joining together vertical sections from successive video frames, each 1 pixel wide and passing through the drop's centre. The camera was recording at 4000 frames per second.

standing wave beneath it is convex, bulging upwards: the drop lands on the crest of its associated wave. Consequently, a small perturbation of the horizontal position of the drop during flight leads to a horizontal component of the reaction force imparted during impact that may destabilize the pure bouncing state.

Below a certain driving threshold, which we denote by the walking threshold Γ_W, the drop's horizontal movement is stabilized by air drag, shear drag in the intervening air layer and the force resulting from the transfer of horizontal momentum imparted by the drop to the surface waves. Mechanically, the latter arises since the

Symbol	Meaning	Typical value
R_0	Drop radius	0.07–0.8 mm
ρ	Silicone oil density	949–960 kg m^{-3}
ρ_a	Air density	1.2 kg m^{-3}
σ	Drop surface tension	20–21 mN m^{-1}
g	Gravitational acceleration	9.81 m s^{-2}
V_{in}	Drop incoming speed	0.1–1 m s^{-1}
V_{out}	Drop outgoing speed	0.01–1 m s^{-1}
μ	Drop dynamic viscosity	10^{-3}–10^{-1} kg m^{-1} s^{-1}
μ_a	Air dynamic viscosity	1.84×10^{-5} kg m^{-1} s^{-1}
ν	Drop kinematic viscosity	10–100 cSt
ν_a	Air kinematic viscosity	15 cSt
T_C	Contact time	1–20 ms
C_R	$= V_{in}/V_{out}$ Coefficient of restitution	0–0.4
f	Bath shaking frequency	40–200 Hz
γ	Peak bath acceleration	0–70 m s^{-2}
ω	$= 2\pi f$ Bath angular frequency	250–1250 rad s^{-}1
ω_D	$= (\sigma/\rho R_0^3)^{1/2}$ Characteristic drop oscillation frequency	300–5000 s^{-1}
We	$= \rho R_0 V_{in}^2/\sigma$ Weber number	0.01–1
Bo	$= \rho g R_0^2/\sigma$ Bond number	10^{-3}–0.4
Oh	$= \mu(\sigma\rho R_0)^{-1/2}$ Drop Ohnesorge number	0.004–2
Oh_a	$= \mu_a(\sigma\rho R_0)^{-1/2}$ Air Ohnesorge number	10^{-4}–10^{-3}
Ω	$= 2\pi f\sqrt{\rho R_0^3/\sigma}$ Vibration number	0–1.4
Γ	$= \gamma/g$ Peak non-dimensional bath acceleration	0–7

TABLE 1. List of symbols used together with typical values encountered in our experiments, as well as those reported in Eddi *et al.* (2011) and Protière *et al.* (2006).

non-axisymmetric deformation of the drop and bath induced by an oblique impact leads to a horizontal pressure gradient in the contact area due to fluid inertia. For $\Gamma > \Gamma_W$, these stabilizing forces can no longer offset the destabilizing wave force and the drop begins to walk. We henceforth shall refer to drops walking in the $(2, 1)$ bouncing mode as *resonant* walkers, because the periodicity of their vertical motion precisely matches that of the Faraday wave field. In certain regimes, the drop then settles into a state of straight-line walking with a steady speed. The walking thresholds have been investigated by Protière *et al.* (2005) for silicone oil with viscosities ranging from $\mu = 10$ to 100 cSt. They found that the walking regime exists only for a small range of driving frequencies, with the typical frequency decreasing with increasing viscosity, as indicated in table 2.

We have measured the walking thresholds for oil with viscosity 20 and 50 cSt, in both cases spanning the whole range of frequencies over which walking occurs. The experimental results are shown in figure 4. The vertical axis denotes the vibration number $\Omega = \omega/\omega_D$, the ratio of the driving angular frequency $\omega = 2\pi f$ to the characteristic oscillation frequency of the drop $\omega_D = (\sigma/\rho R_0^3)^{1/2}$ (see MBI). We first note that the walking threshold curves are composed of two distinct parts joined at $\Gamma_{WM} = \min_\Omega \{\Gamma_W\}$, the minimum driving acceleration required to produce walking. While the lower branches of the threshold curves seem to have similar slopes for all frequencies, the slopes of the upper branches decrease dramatically with increasing frequency, until disappearing completely as f approaches f_{max}. We also observe that the

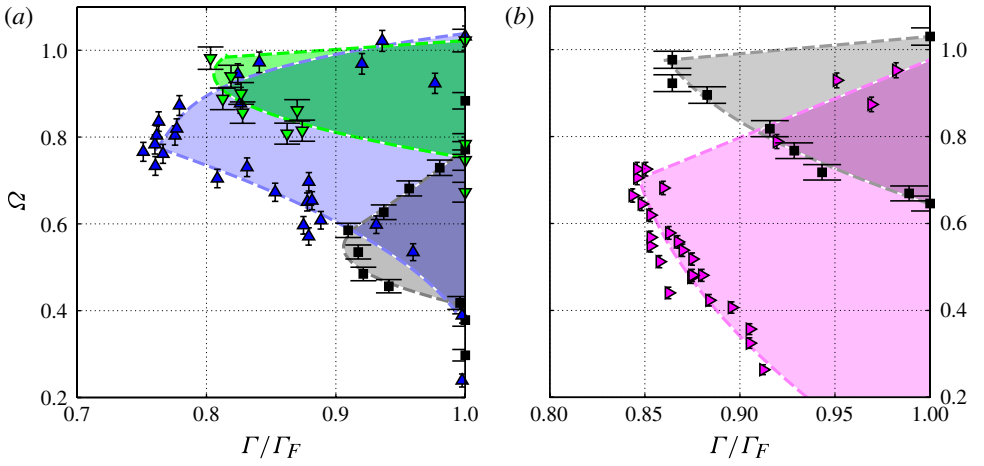

FIGURE 4. (Colour online) The walking thresholds for silicone oil droplets of viscosity (*a*) 20 cSt and (*b*) 50 cSt on a vibrating bath of the same oil. The experimentally measured threshold acceleration $\Gamma = \gamma/g$ (horizontal axis) is shown as a function of the vibration number $\Omega = \omega/\omega_D$ (vertical axis) for several values of the driving frequency f: 50 Hz (▶), 60 Hz (■), 80 Hz (▲) and 90 Hz (▼). The dashed lines are best-fitting curves provided to guide the eye.

Viscosity (cSt)	f_{min} (Hz)	f_{opt} (Hz)	f_{max} (Hz)
10	100	110	125
20	60	80	90
50	40	55	60
100	35	45	50

TABLE 2. The range of driving frequencies for which drops can walk, for various values of the oil viscosity, as reported by Protière *et al.* (2005). Walking occurs for $f_{min} \leqslant f \leqslant f_{max}$, with the minimum value of Γ_W/Γ_F occurring at $f = f_{opt}$. For $f = f_{opt}$, the smallest relative driving acceleration Γ_W/Γ_F is required to produce a walking drop. The resolution of their frequency sweep was 5 Hz.

peak of the walking regime moves to higher Ω with increasing frequency, but never greatly exceeds $\Omega = 1$.

The dependence of the horizontal walking speed on the driving acceleration is shown in figure 5. The walking speed generally increases with increasing drop size, but this trend may be violated for larger drops due to complications associated with the vertical dynamics, an effect to be discussed in § 5.

3. Waves on the bath surface

The purpose of this section is to describe the evolution of the bath deformation caused by a single drop impact. We will assume the deformations to be small and additive, so that the bath shape after multiple drop impacts can be simply obtained by adding the contributions from successive impacts. We are particularly interested in the long-term evolution of the surface waves, which is important in the dynamics

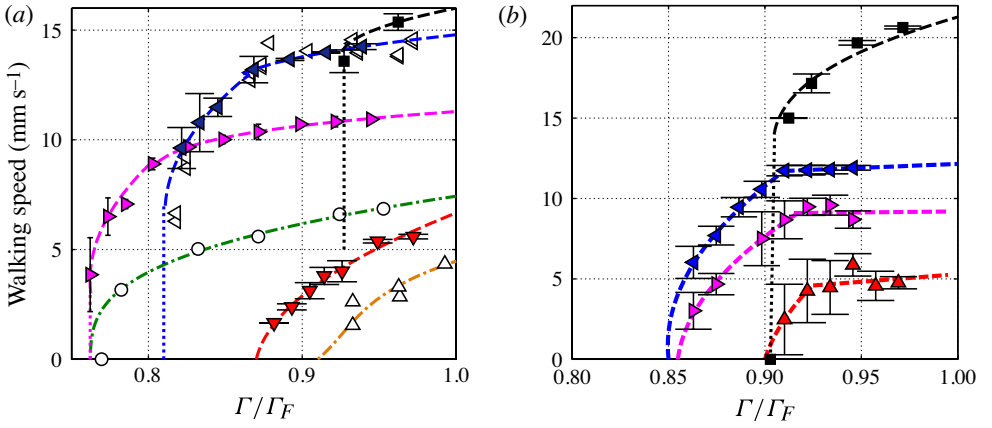

FIGURE 5. (Colour online) The walking speed of silicone oil droplets for (*a*) $\nu = 20$ cSt, $f = 80$ Hz and (*b*) $\nu = 50$ cSt, $f = 50$ Hz, bouncing on a vibrating bath of the same oil, as a function of the driving acceleration. The experimentally measured speeds are shown for several droplet radii R_0. For 20 cSt, $R_0 = 0.31$ mm (▼), 0.38 mm (►), 0.40 mm (◄) and 0.43 mm (■); while for 50 cSt, $R_0 = 0.25$ mm (▲), 0.34 mm (►), 0.39 mm (◄) and 0.51 mm (■). In panel (*a*), the walking speeds reported by Protière *et al.* (2006) are also shown for comparison, for drop radii 0.28 mm (△), 0.35 mm (◯) and 0.41 mm (◁).

of walkers close to the Faraday threshold. Of course, the bath surface profile only influences the drop dynamics when the drop is in contact with the bath; thus, any transient behaviour arising between impacts is irrelevant to our model and need not be considered.

We thus consider a single, normal impact of a liquid drop on a flat vibrating liquid bath. We assume that the drop is initially spherical and therefore the wave field is radially symmetric about the point of impact. The dimensional height of the bath surface will thus depend only on time and distance from the axis of symmetry: $h'(x, y, t) = h'(r', t)$. We non-dimensionalize the governing equations using length and time scales deduced from the drop radius R_0 and the characteristic oscillation frequency of the drop $\omega_D = (\sigma/\rho R_0^3)^{1/2}$:

$$h = h'/R_0, \quad r = r'/R_0, \quad \tau = \omega_D t = t(\sigma/\rho R_0^3)^{1/2}, \quad Z = z/R_0, \quad k = k'R_0. \tag{3.1}$$

The Hankel transform $H(k, \tau)$ of the dimensionless surface height $h(r, \tau)$ is defined by

$$H(k, \tau) = \int_0^\infty h(r, \tau) \mathrm{J}_0(kr) r \, \mathrm{d}r \quad \text{so that } h(r, \tau) = \int_0^\infty H(k, \tau) \mathrm{J}_0(kr) k \, \mathrm{d}k. \tag{3.2}$$

Here, and throughout the paper, $\mathrm{J}_i(x)$ denotes the Bessel function of the first kind and order i. The effective gravity in the bath frame of reference, defined as the sum of gravity and the fictitious force arising in this vibrating reference frame, is given by

$$Bo^*(\tau) = Bo(1 + \Gamma \sin \Omega\tau). \tag{3.3}$$

In the frame of reference fixed with the oscillating bath, the quiescent bath surface is located at $Z = 0$ at all times. The vertical position $Z(\tau)$ of the drop will be represented by its centre of mass shifted down by one radius, so that $Z(\tau) = 0$ when the drop first

makes contact with the unperturbed bath. Then $Z(\tau)$ is governed by

$$\frac{\partial^2 Z}{\partial \tau^2} = F(\tau) - Bo^*(\tau), \tag{3.4}$$

where F is the dimensionless reaction force acting on the drop. The Hankel transform of the surface height can be modelled by

$$H_{\tau\tau} + 2Oh_e k^2 H_\tau + H[k^3 + kBo^*(\tau)] = -\frac{4}{3}F(\tau)\frac{\mathrm{J}_1(wk)}{w}, \tag{3.5}$$

where w is the dimensionless extent of the contact region and $Oh_e = \mu_e/(\sigma\rho R_0)^{1/2}$ is an effective Ohnesorge number (see the Appendix, § A.2). When $Bo \ll 1$, we can approximate the forcing term in (3.5) by a point forcing (see § A.3) and so obtain

$$H_{\tau\tau} + 2Oh_e k^2 H_\tau + H(k^3 + kBo^*(\tau)) = -\tfrac{2}{3}kF(\tau). \tag{3.6}$$

In § A.4 we analyse the long-term evolution of the bath surface following a single drop impact when the forcing is close to the Faraday threshold Γ_F. We find (see (A 50)) that the impact creates a standing wave with nearly sinusoidal time dependence and Bessel function spatial dependence, which decays exponentially in time. The rate of decay is proportional to the relative distance from the Faraday threshold $1-\Gamma/\Gamma_F$. The amplitude of the wave is given by the integral of the reaction force F over the contact time, multiplied by the Green's function for (3.5), which is approximately $\sin(\Omega\tau/2)$:

$$h(r,\tau) \approx \frac{4\sqrt{2\pi}}{3\sqrt{\tau}}\frac{k_C^2 k_F Oh_e^{1/2}}{3k_F^2 + Bo}\left[\int_{\tau_C} F(u)\sin\frac{\Omega u}{2}\,\mathrm{d}u\right]\cos\frac{\Omega\tau}{2}\exp\left\{\left(\frac{\Gamma}{\Gamma_F}-1\right)\frac{\tau}{\tau_D}\right\}\mathrm{J}_0(k_C r). \tag{3.7}$$

The critical (most unstable) wavenumber k_C is found to be close to the Faraday wavenumber k_F, given by the dispersion relation (Benjamin & Ursell 1954)

$$k_F^3 + Bok_F = \tfrac{1}{4}\Omega^2. \tag{3.8}$$

Equation (3.7) is found to be a good approximation provided that $(\mu^3 f/\rho\sigma^2)^{1/3} \ll 2$ (A 51), which is satisfied for the parameter range of interest. In order to obtain a closer match with experimental data, the analytic expression (3.7) is superseded by a slightly more complex relation, derived in § A.5 using a more complete description of the wave field:

$$h(r,\tau) \approx \frac{4\sqrt{2\pi}}{3}\frac{k_C^2 k_F Oh_e^{1/2}}{3k_F^2 + Bo}\left[\int F(u)\sin\frac{\Omega u}{2}\,\mathrm{d}u\right]\frac{\bar{H}(\tau)}{\sqrt{\tau}}\exp\left\{\left(\frac{\Gamma}{\Gamma_F}-1\right)\frac{\tau}{\tau_D}\right\}\mathrm{J}_0(k_C r), \tag{3.9}$$

with $\bar{H}(\tau)$, k_c and τ_D now determined by a numerical scheme described in § A.5. To illustrate the accuracy of (3.9), we compare it to a full numerical solution of (3.6) in figure 6.

4. Horizontal dynamics

In this section, we combine our models for the vertical drop dynamics (from MBI) and the standing-wave evolution (from § 3) in order to describe the complete drop dynamics. The model presented here is readily generalizable to a full three-dimensional model; however, experimental evidence indicates the prevalence of a

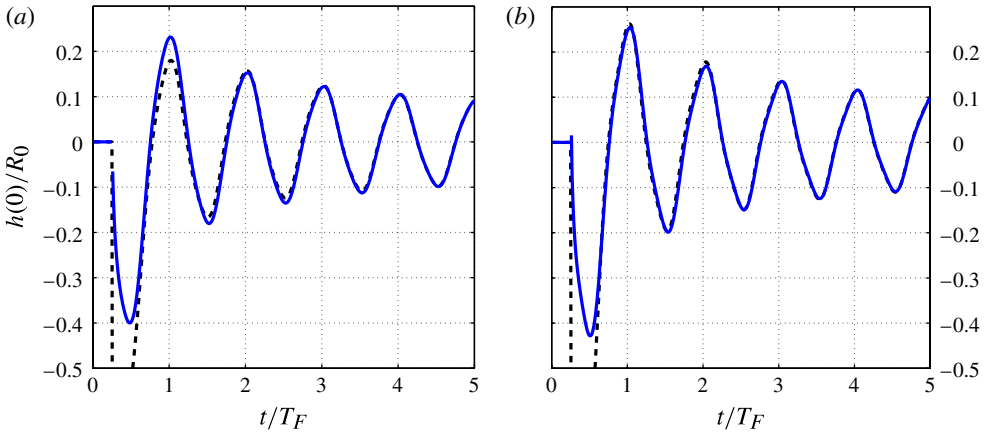

FIGURE 6. (Colour online) Comparison between the full numerical model (dashed line) and the long-term approximation (A 50) (solid line) for (*a*) 20 cSt oil at 80 Hz and (*b*) 50 cSt oil at 50 Hz. The dimensionless height of the surface $h(0, \tau)$ at the centre of drop impact is shown as a function of time, non-dimensionalized by the Faraday period $T_F = 2/f$. The surface is forced at $t = T_F/4$ and then evolves freely.

two-dimensional motion, in which the drop is confined within a vertical plane unless perturbed transversely by an external force or through interaction with boundaries. We thus expect that a two-dimensional model will suffice in describing the behaviour of a drop bouncing on an unbounded vibrating liquid bath.

We non-dimensionalize the position and time as in § 3, and denote the horizontal drop position by $X(\tau) = x(\tau)/R_0$.

4.1. *Horizontal drag during contact*

All previous models of walking drops have assumed, following the argument first proposed by Protière *et al.* (2006), that the shearing inside the intervening air layer provides the principal contribution to the horizontal drag during impact. Instead, we propose that the dominant contribution comes from the direct transfer of momentum from the drop to the bath during impact. The resulting horizontal force is difficult to characterize analytically or numerically, owing to the asymmetry of the drop and bath surfaces involved, but the resulting tangential coefficient of restitution $C_R^T = v_{out}^T/v_{in}^T$ is straightforward to measure experimentally.

We have recorded C_R^T for silicone oil drops with $0.1\ \text{mm} \leqslant R_0 \leqslant 0.6\ \text{mm}$, $\nu = 20$ and 50 cSt and a wide range of normal and tangential velocities ($0.01\ \text{m s}^{-1} \leqslant v_{in}^T, v_{in}^N \leqslant 0.8\ \text{m s}^{-1}$). The results are shown in figure 7 as a function of the normal Weber number $We^N = \rho R_0 (v_{in}^N)^2/\sigma$. The data indicate that C_R^T depends only weakly on the oil viscosity. Note that we have controlled neither the tangential velocity v_{in}^T nor the normal velocity v_{in}^N, and the incident angle θ thus ranged from nearly 90° (for normal impact) to 45°. The near collapse of the data onto a single curve implies that, over the parameter regime of interest, C_R^T does not depend appreciably on either θ or v_{in}^T, which indicates that the tangential drag force depends linearly on v_{in}^T. We conclude that the dimensionless tangential force on the drop $\bar{F}_D$ is a function of the drop position Z, normal velocity Z_τ and the normal force F, multiplied by the tangential velocity: $\bar{F}_D = C(Z, Z_\tau, F)X_\tau$. For the sake of simplicity, we assume $\bar{F}_D = CF^aX_\tau$. The coefficients C and a can be determined by matching the experimental data; the best

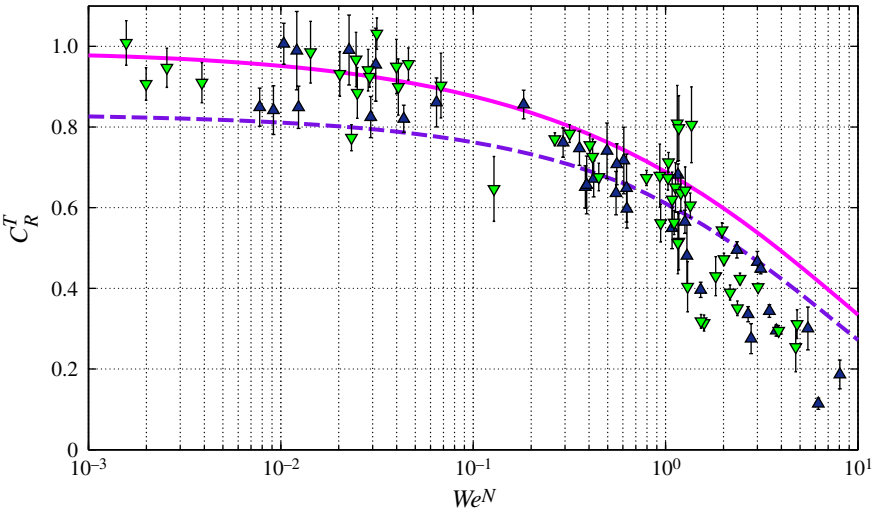

FIGURE 7. (Colour online) The tangential coefficient of restitution $C_R^T = v_{out}^T/v_{in}^T$ as a function of the normal Weber number $We^N = \rho R_0 (v_{in}^N)^2/\sigma$, where v^T and v^N are the tangential and normal components of the drop velocity relative to the bath surface. Data for 20 cSt (▼) and 50 cSt (▲) silicone oil are shown, together with the values obtained with the model (4.1) with $C = 0.3$ for $R_0 = 0.1$ mm (solid line) and $R_0 = 0.4$ mm (dashed line). The impact angle with respect to the bath surface ranged from 45° to nearly 90°.

match is achieved for $1 \lesssim a \lesssim 1.5$. We shall use $a = 1$, and so write

$$\bar{F}_D = CFX_\tau \quad \text{where } F = Z_{\tau\tau} + Bo^*. \tag{4.1}$$

The experimental data are best fitted by choosing $C = 0.3$, as is shown in figure 7, where the two curves indicate the model predictions for $R_0 = 0.1$ mm and $R_0 = 0.3$ mm. Using the shearing force in the air layer as the dominant drag force gives $\bar{F}_D \sim F^{1/2}$, leading to an underestimation of the tangential drag for high Weber numbers (since $F^{1/2} < F$).

4.2. *Horizontal drag during flight*

When the drop is in flight (specifically, not experiencing a reaction force from the bath), its dynamics may be approximated by the system

$$X_{\tau\tau} = -F_{DA}(\bar{V})\frac{X_\tau}{\bar{V}}, \tag{4.2a}$$

$$Z_{\tau\tau} = -Bo^*(\tau) - F_{DA}(\bar{V})\frac{Z_\tau}{\bar{V}}, \tag{4.2b}$$

where, as previously, $Bo^*(\tau) = Bo(1 + \Gamma \sin \Omega\tau)$ is the effective gravity in our vibrating frame of reference, $\bar{V} = (X_\tau^2 + Z_\tau^2)^{1/2}$ is the dimensionless droplet speed, and F_{DA} is the air drag. We assume that the drag is always opposite to the velocity and that its magnitude is a function of speed only, thus neglecting the effect of the bath on the air flow around the drop (Goldman, Cox & Brenner 1967). The maximum value of the Reynolds number $Re_{max} = 2R_0V_{max}/\nu_a = 2gR_0/f\nu_a$ varies between 4 for $f = 100$ Hz and $R_0 = 0.3$ mm and 16 for $f = 40$ Hz and $R_0 = 0.5$ mm, so the Stokes formula for

the air drag on a rigid sphere is no longer accurate. Moreover, the motion of the drop is unsteady, and we need to take into account the variable flow profile around the drop. The Strouhal number $St = \omega R_0/V_{max} = \pi R_0 f^2/g$, a measure of the flow unsteadiness, is typically between 0.1 and 1 in our system. Chang & Maxey (1994) showed that the relative magnitude of the correction to the Stokes drag is of the order of $ReSt/6$ when both of these dimensionless numbers achieve small or moderate values:

$$F_{DA} = \tfrac{9}{2} Oh_a \bar{V}[1 + O(\tfrac{1}{6} ReSt)]. \tag{4.3}$$

We shall show that the correction in (4.3) is negligible in its effect on the horizontal drop dynamics relative to the sum of the Stokes drag and the momentum drag during impact. To that end, we average the horizontal equation of motion over the period of the drop's motion P, giving us the average drag on the drop. Integrating (4.1), we derive that the momentum drag contribution to the average drag scales like $X_\tau C(\int F)/P = CX_\tau Bo$, since by periodicity the integral of the reaction force on the drop $\int F$ must equal the integral of the gravitational force $\int Bo = BoP$ over the period. The contribution of the air drag scales simply like $X_\tau[\frac{9}{2} Oh_a + O(\frac{3}{4} Oh_a ReSt)]$. The relative magnitude of the Stokes drag to the momentum drag contribution is therefore given by $9Oh_a/2CBo \approx 20\mu_a \sigma^{1/2} \rho^{-3/2} g^{-1} R_0^{-5/2}$, which varies between 0.36 for $R_0 = 0.2$ mm and 0.02 for $R_0 = 0.6$ mm. As expected, the air drag plays a much smaller role for larger drops and is never the dominant source of momentum loss, but for drops below $R_0 = 0.4$ mm it cannot be neglected. However, the relative magnitude of the air drag correction to the momentum drag, given by $3Oh_a ReSt/4CBo = 25\rho_a \sigma^{1/2} f \rho^{-3/2} g^{-1} R_0^{-1/2}$, varies between 0.08 for $R_0 = 0.2$ mm and $f = 80$ Hz and 0.03 for $R_0 = 0.6$ mm and $f = 50$ Hz. Therefore, we shall from now on neglect the correction term.

It is also straightforward to check that in the vertical direction the drag is negligible relative to gravity, their ratio being at most $9\mu_a/2\rho f R_0^2$, which is at most 0.04 for $R_0 \geqslant 0.2$ mm and $f \geqslant 50$ Hz. Therefore (4.2) can be simplified to

$$X_{\tau\tau} = -\tfrac{9}{2} Oh_a X_\tau, \quad Z_{\tau\tau} = -Bo^*(\tau). \tag{4.4}$$

4.3. *Horizontal kick*

The remaining force to be evaluated is the horizontal component of the reaction force, arising due to the slope of the wave field beneath the drop. It is important to clarify the somewhat artificial distinction between the reaction and drag forces. By the reaction force, we mean that part of the total force on the drop during contact that is independent (to leading order) of the drop's horizontal velocity. Conversely, the drag component was found to scale linearly with the drop's horizontal speed. Had the drop impact been instantaneous, the tangential component of the reaction force could be obtained from its vertical component simply by calculating the slope of the interface at the position of the drop:

$$\bar{F}_T = -\frac{\partial h(X,\tau)}{\partial X} F, \tag{4.5}$$

assuming a small slope (so that $\sin\theta \approx \theta$ for the slope angle). Such an approximation loses accuracy when the contact time of the drop becomes comparable to the Faraday period, because the slope of the interface changes significantly during contact. The interplay between the interface deformation beneath the drop and its changing slope further away is far from trivial. Unless one can afford to numerically model the whole complex dynamics of this interaction (which would decrease the speed of computation

by many orders of magnitude), one can do no better than calculate a weighted average of the slope over the contact time. The average slope weighted by the instantaneous reaction force (4.5) is the most natural and yields the best results; thus, it will be adopted in our model. However, the predictions obtained using this model for $\Omega \gtrsim 1$ or for the $(2,1)^1$ walking mode are likely to be skewed, due to the contact time extending over a relatively large fraction of the Faraday period.

4.4. *Summary of the model*

The vertical dynamics of the drop is governed by the logarithmic spring model developed in MBI in order to capture the dynamics of drop rebound on a liquid bath for Weber numbers ranging from small to moderate ($We \lesssim 3$). It was derived using a variational approach by assuming a quasi-static form for both the drop and interface shapes during impact. The dimensional form of the model equations is presented in (4.6) below. When the drop is in flight, it is acted upon only by the effective gravity (gravity plus the fictitious force in the vibrating bath reference frame), with air drag being negligible. During contact, the drop also feels a reaction force dependent on the relative position of the drop and bath height $z-h$, as well as a drag dependent on the relative speed of the drop and bath $\dot{z}-\dot{h}$. Unlike for a linear spring model, the dependence of the reaction force on the relative position and of the drag on the relative speed is not linear, as evidenced by the logarithmic correction in (4.6). This nonlinearity has the effect of reducing dissipation and prolonging contact for smaller impact speeds. There is also a correction to the drop inertia coming from the drop's internal fluid motion. The three coefficients c_i present in the model were fixed by matching the experimentally measured coefficients of restitution and contact times, as described in MBI. The model was shown to accurately predict the regime diagrams of the drop's vertical bouncing motion. Writing m for the drop mass, $g^*(t) = g + \gamma \sin(2\pi f t)$ for the gravitational acceleration in the vibrating bath frame of reference, and $F_N = m\ddot{z} + mg^*(t)$ for the normal component of the reaction force acting on the drop, we have

$$m\ddot{z} = -mg^*(t) \quad \text{in flight,} \tag{4.6a}$$

$$\left(1 + \frac{c_3}{\ln^2\left|\dfrac{c_1 R_0}{z-h}\right|}\right) m\ddot{z} + \frac{4}{3}\frac{\pi\mu R_0 c_2(\nu)}{\ln\left|\dfrac{c_1 R_0}{z-h}\right|}(\dot{z}-\dot{h}) + \frac{2\pi\sigma(z-h)}{\ln\left|\dfrac{c_1 R_0}{z-h}\right|} = -mg^*(t) \quad \text{otherwise.} \tag{4.6b}$$

The drop is defined to be in flight either when $z \geqslant h$ or when F_N, as computed from (4.6*b*), would return a negative value. The constants used here, as in MBI, were $c_1 = 2$, $c_3 = 1.4$ and $c_2 = 12.5$ for 20 cSt and $c_2 = 7.5$ for 50 cSt. These values can be determined either by matching the known normal coefficient of restitution C_R^N and contact time T_C of the drop and their dependence on We, or by fitting the regime diagrams of the vertical bouncing motion, as was done in MBI. The total height of the standing waves in the bath frame of reference $h = h(X,\tau)$ can be expressed as the sum of contributions from all previous impacts:

$$h(x,t) = \sum_{n=1}^{N} h_0(x, x_n, t, t_n). \tag{4.7}$$

The single contribution $h_0(x, x_n, t, t_n)$ resulting from an impact at $(x, t) = (x_n, t_n)$ is given by the long-time approximation (A 52):

$$h_0(x, x_n, t, t_n) \approx \sqrt{\frac{2}{\pi}} \frac{k_F R_0}{3k_F^2 R_0^2 + Bo} \frac{R_0 k_C^2 \mu_e^{1/2}}{\sigma} \left[\int F_N(t') \sin(\pi f t') \, \mathrm{d}t' \right] \times \frac{\bar{H}(t)}{\sqrt{t - t_n}} \exp\left\{ (\Gamma/\Gamma_F - 1) \frac{t - t_n}{T_d} \right\} \mathrm{J}_0(k_C(x - x_n)). \tag{4.8}$$

In order to increase computational speed, the number of previous impacts stored is kept to a manageable size by discarding those whose standing-wave amplitude has decayed sufficiently (below 0.1 % of its initial value). Since the contact takes place over a finite length of time, x_n and t_n are taken as the weighted averages of x and t over the contact time:

$$x_n = \int_{t_c} F_N(t') x(t') \, \mathrm{d}t' \Big/ \int_{t_c} F_N(t') \, \mathrm{d}t', \quad t_n = \int_{t_c} F_N(t') t' \, \mathrm{d}t' \Big/ \int_{t_c} F_N(t') \, \mathrm{d}t'. \tag{4.9}$$

Finally, the horizontal dynamics is governed by

$$m\ddot{x} + D(t)\dot{x} = -h_x F_N, \tag{4.10}$$

where $D(t) = C\sqrt{\rho R_0/\sigma} F_N(t) + 6\pi R_0 \mu_a$ is the total instantaneous drag coefficient and C is the proportionality constant for the tangential drag force. If our model is correct, the value of C should be close to 0.3. In fact, we expect it to be slightly less than 0.3, as the tangential coefficient of restitution measured experimentally also includes the contribution from the shearing in the intervening air layer. This contribution is presumably smaller for walking drops, which, after repeated impacts on the bath with associated shear torques, should acquire a rotation that would reduce the relative velocity of the two surfaces during contact.

4.5. *Analysis for small drops*

We now simplify (4.8)–(4.10) by assuming that the drop is in the $(2, 1)^2$ mode and $\Omega \ll 1$, which means that the drop is bouncing periodically with the Faraday period $T_F = 2/f$ and the contact time per period is much shorter than T_F. It follows that $\int_t^{t+T_F} F_N(t') \, \mathrm{d}t' = \int_t^{t+T_F} m\ddot{z}(t) + mg^*(t') \, \mathrm{d}t' = \dot{z}|_t^{t+T_F} + mgT_F = mgT_F$. We can define the phases Φ_i^1 and Φ_i^2 as follows:

$$\int F_N(t') \sin(\pi f t') \, \mathrm{d}t' = \left[\int F_N(t') \, \mathrm{d}t' \right] \sin \frac{\Phi_i^1}{2} = mgT_F \sin \frac{\Phi_i^1}{2}, \tag{4.11a}$$

$$\int F_N(t') \cos(\pi f t') \, \mathrm{d}t' = \left[\int F_N(t') \, \mathrm{d}t' \right] \cos \frac{\Phi_i^2}{2} = mgT_F \cos \frac{\Phi_i^2}{2}. \tag{4.11b}$$

Thus, $\sin(\Phi_i^1/2)$ is the weighted average of $\sin(\pi f t)$ over the duration of the contact, and similarly $\cos(\Phi_i^2/2)$ is the weighted average of $\cos(\pi f t)$. For small Ω, the contact time is sufficiently short that we have $\Phi_i^1 \approx \Phi_i^2$. We then define the phase of impact Φ_i by the following relation:

$$\sin \Phi_i = 2 \sin \frac{\Phi_i^1}{2} \cos \frac{\Phi_i^2}{2}. \tag{4.12}$$

Approximating k_C by k_F and $\bar{H}(t)$ by $\cos(\pi f t)$ as in (A 49), we can write (4.8) as

$$h_0(x, x_n, t, t_n) \approx A \sin\frac{\Phi_i^1}{2}\frac{\cos(\pi f t)}{\sqrt{t-t_n}} \exp\left\{(\Gamma/\Gamma_F - 1)\frac{t-t_n}{T_d}\right\} \mathrm{J}_0(k_F(x-x_n)),$$

$$\text{where} \quad A = \sqrt{\frac{2}{\pi}}\frac{k_F R_0}{3k_F^2 R_0^2 + Bo}\frac{R_0 k_F^2 \mu_e^{1/2}}{\sigma\rho^{1/2}} mgT_F. \tag{4.13}$$

Following Eddi *et al.* (2011) we introduce the dimensionless 'memory' parameter

$$\mathscr{M}_e = \frac{T_d}{T_F(1-\Gamma/\Gamma_F)}, \tag{4.14}$$

which prescribes the inverse of the decay rate of the waves and so the number of the previous impacts that significantly contribute to the overall surface deformation. Assuming that the drop's horizontal speed varies on a time scale that is much longer than the bouncing period, we can integrate (4.10) over one period to obtain

$$m\ddot{x} + \bar{D}\dot{x} = -mg\frac{\partial h}{\partial x} = -\frac{1}{2}Amg\sin\Phi_i \frac{\partial}{\partial x}\sum_{n=1}^{N}\frac{\mathrm{e}^{-n/\mathscr{M}_e}}{\sqrt{nT_F}}\mathrm{J}_0(k_F(x-x_n)), \tag{4.15}$$

where $\bar{D} = C\sqrt{\rho R_0/\sigma}\, mg + 6\pi R_0\mu_a$ is the average horizontal drag coefficient. We have used (4.12) and the assumption that the contact time is much smaller than T_F, approximating $t' - t_n$ by $t_{N+1} - t_n$. We have also reversed the sequences $\{x_n\}$ and $\{t_n\}$, so that (x_1, t_1) now corresponds to the most recent impact. We can easily generalize (4.15) to the case of a drop walking in a plane rather than a line, by replacing $\partial/\partial x$ with $\boldsymbol{\nabla}$:

$$m\ddot{\boldsymbol{x}} + \bar{D}\dot{\boldsymbol{x}} = -mg\boldsymbol{\nabla}h = -\frac{1}{2}Amg\sin\Phi_i\,\boldsymbol{\nabla}\sum_{n=1}^{N}\frac{\mathrm{e}^{-n/\mathscr{M}_e}}{\sqrt{nT_F}}\mathrm{J}_0(k_F(\boldsymbol{x}-\boldsymbol{x}_n)), \tag{4.16}$$

which represents the walker's horizontal trajectory equation.

Now we assume that the drop is walking horizontally with steady average speed v, so that $x(t+T_F) - x(t) = vT_F$. We can then rewrite (4.15) as

$$\bar{D}v = \frac{1}{2}Amgk_F\sin\Phi_i\sum_{n=1}^{N}\frac{\mathrm{e}^{-n/\mathscr{M}_e}}{\sqrt{nT_F}}\mathrm{J}_1(nk_F T_F v). \tag{4.17}$$

In order to simplify the subsequent equations, we here neglect the contribution of the air drag to the total average drag $\bar{D}$, and derive

$$v = \sqrt{\frac{\sigma}{\rho R_0}}\frac{Ak_F\sin\Phi_i}{2CT_F^{1/2}}\sum_{n=1}^{\infty}\mathrm{e}^{-n/\mathscr{M}_e}n^{-1/2}\mathrm{J}_1(nk_F T_F v). \tag{4.18}$$

In (4.18), only $\mathscr{M}_e$ and Φ_i depend on the bath acceleration. While $\mathscr{M}_e$ depends strongly on the distance from threshold, Φ_i changes more gradually, with values generally in the range $0.25 < \sin\Phi_i < 0.65$. For the sake of simplicity, at this stage we set $\sin\Phi_i$ to be a constant. Finally, we use $C = 0.2$, a value that is found to best fit the data (see § 5). After all the aforementioned simplifications, we are left with a relatively simple expression for the horizontal particle speed:

$$v = \frac{5}{2}\sqrt{\frac{\sigma}{\rho R_0}}A\sin\Phi_i\, k_F T_F^{-1/2}\sum_{n=1}^{\infty}\mathrm{e}^{-n/\mathscr{M}_e}n^{-1/2}\mathrm{J}_1(nk_F T_F v). \tag{4.19}$$

For small values of $\mathscr{M}_e$ (far from the Faraday threshold), (4.19) has only one solution, $v = 0$, i.e. a droplet bouncing with no lateral motion. When the memory increases above a critical value $\mathscr{M}_e^c$, however, the zero solution becomes unstable and a pair of non-zero solutions appear (one negative, one positive). It is possible to obtain an approximation to $\mathscr{M}_e^c$ by taking the limit $v \to 0$ (i.e. approaching the critical value from above), or equivalently $\mathrm{J}_1(nk_FT_Fv) \to nk_FT_Fv/2$ for each n, which means that (4.19) is satisfied for

$$v = 0 \quad \text{or} \quad 1 = \frac{5}{4}\sqrt{\frac{\sigma}{\rho R_0}}\, A \sin\Phi_i\, k_F^2 T_F^{1/2} \sum_{n=1}^{\infty} \mathrm{e}^{-n/\mathscr{M}_e} n^{1/2}. \tag{4.20}$$

Then $\mathscr{M}_e^c$ is the value of $\mathscr{M}_e$ for which the latter equality is satisfied. We approximate the infinite sum

$$\sum_{n=1}^{\infty} \mathrm{e}^{-n/\mathscr{M}_e} n^{1/2} = \int_0^{\infty} \mathrm{e}^{-x/\mathscr{M}_e} x^{1/2}\, \mathrm{d}x (1 + \mathrm{O}(\mathscr{M}_e^{-1})) \approx \Gamma\left(\frac{3}{2}\right) \mathscr{M}_e^{3/2}, \tag{4.21}$$

and so deduce

$$\mathscr{M}_e^c \approx \left[\frac{\sqrt{\pi}}{2}\frac{5}{4} A \sin\Phi_i\, k_F^2 \sqrt{\frac{\sigma T_F}{\rho R_0}}\right]^{-2/3} = \left[\frac{5\sqrt{2}\,\pi \sin\Phi_i (k_F R_0)^5}{6(3k_F^2R_0^2 + Bo)} \sqrt{\frac{\mu_e g^2 T_F^3}{\sigma R_0}}\right]^{-2/3}. \tag{4.22}$$

By combining (4.22) with (4.14), we can derive an approximation to the walking threshold Γ_W, while (4.19) enables us to calculate the dependence of the walking speed v on the driving acceleration. The comparison of the predictions for this small-drop regime with experimental results is shown in figures 8 and 9. We note that, without the detailed knowledge of $\sin\Phi_i$ (we used a constant value), the predictions are not entirely satisfactory. Although in figure 8 we see that the predicted walking threshold does shift to higher Ω with increasing frequency, the change is not sufficiently large. Moreover, we cannot capture the finite size of the walking regime, specifically its confinement to $\Omega \lesssim 1$, without considering the switching of vertical bouncing modes.

In figure 9, we compare the predicted walking speed dependence on driving acceleration with the experimental data. By choosing the phase Φ_i appropriately, we can match the data for at least one drop size. However, the match for the other drop sizes is then rather poor, with the model being too insensitive to drop size for 20 cSt (figure 9*a*) and too sensitive for 50 cSt (figure 9*b*). Additionally, the slopes of the experimentally measured curves decrease for larger driving accelerations, while the theoretical curves show no such trend. This discrepancy can largely be attributed to the gradual change of phase with increasing driving acceleration, a necessary implication of the periodicity condition. Furthermore, in figure 9(*b*) the phase changes discontinuously around $\Gamma \approx 0.92\Gamma_F$ due to a transition between the $(2, 1)^1$ and $(2, 1)^2$ walking modes (see § 5).

5. Results

The results of our theoretical model from § 4.4 are shown in figures 10–15. In figures 10–13, the value of the tangential drag coefficient C in (4.10) was fitted for each combination of frequency and viscosity in order to obtain the best match with experimental data, as shown in table 3. The coefficient C remained in the interval $[0.17, 0.33]$, which is roughly consistent with the experimentally obtained upper bound

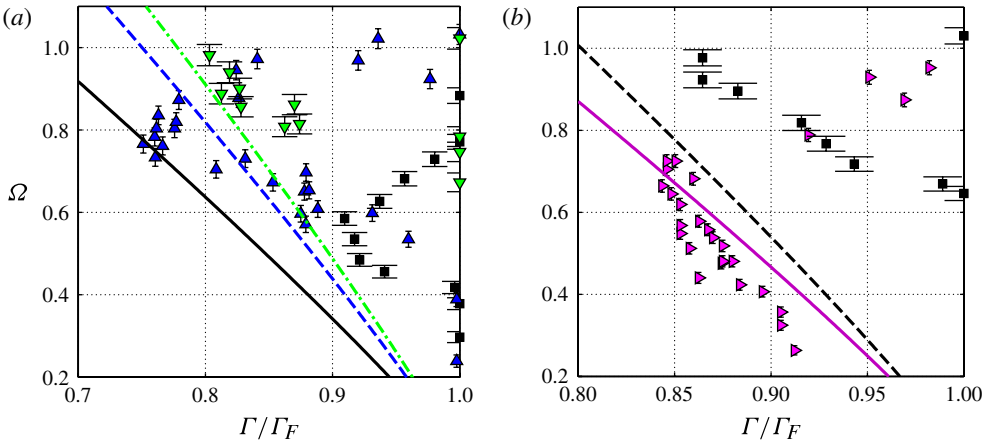

FIGURE 8. (Colour online) The walking thresholds as predicted by (4.22) for (*a*) 20 cSt droplets at driving frequency $f = 60$ Hz (solid line), 80 Hz (dashed line) and 90 Hz (dash-dotted line) and (*b*) 50 cSt droplets at $f = 50$ Hz (solid line) and 60 Hz (dashed line). These should be compared to the corresponding experimental data at driving frequency $f = 50$ Hz (►), 60 Hz (■), 80 Hz (▲) and 90 Hz (▼).

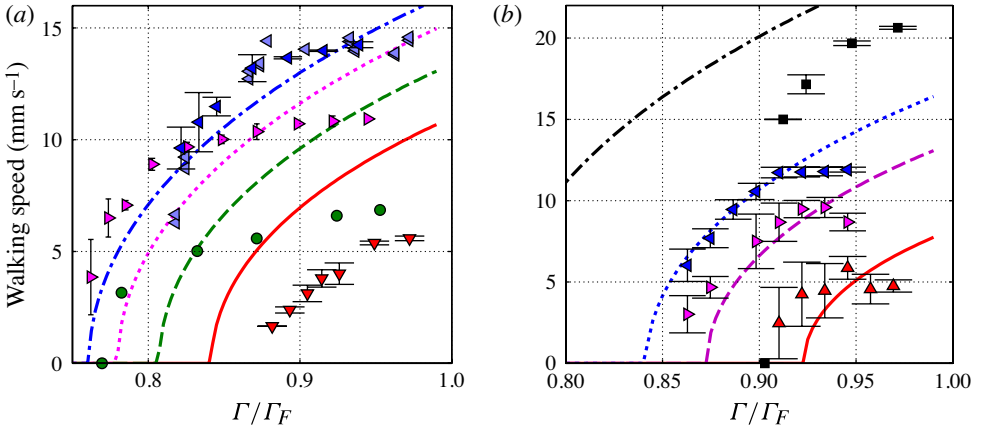

FIGURE 9. (Colour online) The walking speeds of silicone oil droplets for (*a*) $\nu = 20$ cSt at $f = 80$ Hz and (*b*) $\nu = 50$ cSt at $f = 50$ Hz, as a function of the driving acceleration relative to the Faraday threshold Γ/Γ_F. In panel (*a*), the experimental data for $R_0 = 0.31$ mm (▼), 0.35 mm (●), 0.38 mm (►) and 0.40 mm (◄) are compared to the speeds obtained using (4.19) with $\sin\Phi_i = 0.5$. In panel (*b*), the experimental data for $R_0 = 0.25$ mm (▲), 0.34 mm (►), 0.39 mm (◄) and 0.51 mm (■) are compared to the predictions of (4.19) with $\sin\Phi_i = 0.7$.

of 0.3. The value for $\nu = 50$ cSt and $f = 60$ Hz is slightly higher than the rest, presumably because it lies close to the limits of validity (see (A 51)) of our long-time approximation of the standing-wave field (A 52).

In figure 10, we show the predicted walking regimes for the two viscosities and several driving frequencies. The solid lines indicate the outer limits of the walking regimes, which for lower frequencies extend as far as the Faraday threshold. For

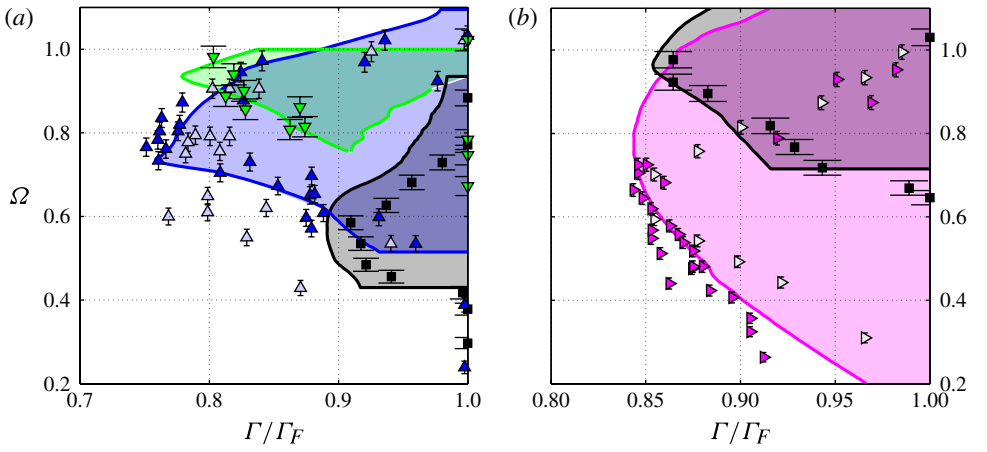

FIGURE 10. (Colour online) The walking thresholds for silicone oil droplets of viscosity (*a*) 20 cSt and (*b*) 50 cSt on a vibrating bath of the same oil. Our model predictions (lines) are compared to the existing data in the Γ/Γ_F–Ω plane, where Γ/Γ_F is the ratio of the peak driving acceleration to the Faraday threshold and $\Omega = \omega/\omega_D$ is the vibration number. Experimental data are shown for several driving frequencies f: 50 Hz (▶) (▷, data from Protière *et al.* (2006)), 60 Hz (■), 80 Hz (▲) (△, data from Eddi *et al.* (2008)) and 90 Hz (▼).

ν (cSt)	f (Hz)	Coefficient C	ν (cSt)	f (Hz)	Coefficient C
20	60	0.21	50	40	0.21
20	80	0.17	50	50	0.17
20	90	0.21	50	60	0.33

TABLE 3. The values of the tangential drag coefficient C used for the different combinations of oil viscosity ν and driving frequency f in our simulations.

higher frequencies (e.g. $f = 90$ Hz, $\nu = 20$ cSt) such is not the case, as the vertical dynamics becomes chaotic for $\Gamma < \Gamma_F$. We note that, while it is possible to have drops walking above the Faraday threshold, the motion is highly irregular, since the wave field is no longer prescribed by the impacts of the drop alone, with Faraday waves arising throughout the container.

In figure 11, we show the regime diagram of the drop's horizontal and vertical motion for $\nu = 20$ cSt silicone oil and several values of frequencies for which walking occurs. The walking regime, denoted $\boldsymbol{W}$, is located in the region where one of the $(2, 1)$ modes is stable sufficiently close to the Faraday threshold to create long-lived standing waves. As the driving frequency is increased, the walking regime moves to higher Ω and decreases in size until it disappears completely. Conversely, as the driving frequency is reduced, the Faraday threshold decreases and penetrates further into the region of steady $(2, 1)$ bouncing. For sufficiently low frequency, the Faraday threshold is lower than the minimum driving acceleration required to sustain a period-doubled mode and the walking region disappears entirely. Therefore, walking occurs only in a finite interval of driving frequencies.

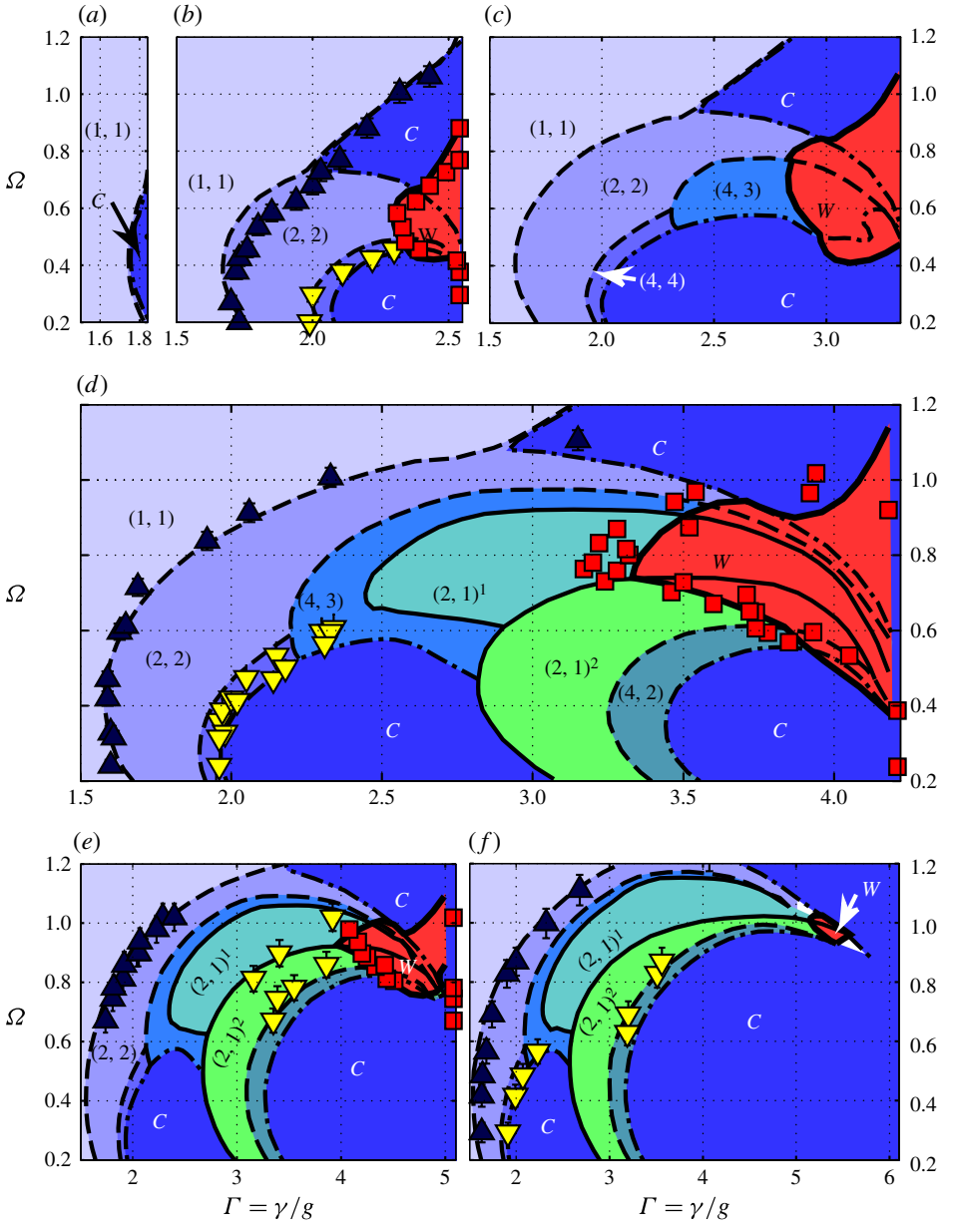

FIGURE 11. (Colour online) Regime diagrams delineating the dependence of the form of the drop's vertical and horizontal motion on the forcing acceleration $\Gamma = \gamma/g$ and the vibration number Ω. Silicone oil of viscosity 20 cSt is considered and several values of the driving frequency f: (*a*) 50 Hz, (*b*) 60 Hz, (*c*) 70 Hz, (*d*) 80 Hz, (*e*) 90 Hz and (*f*) 100 Hz. The walking regime (W) occurs primarily within the (2, 1) bouncing mode regimes, and a sharp change in the slope of its boundary is evident across the border between the $(2, 1)^1$ and $(2, 1)^2$ modes. The walking regime, whose extent is seen to depend strongly on f, generally borders on chaotic bouncing regions (C), both above and below. Where available, experimental data on the first (▲) and second (▼) period doubling and on the walking thresholds (■) are also shown. The rightmost boundary corresponds to the Faraday threshold Γ_F. Characteristic error bars are shown.

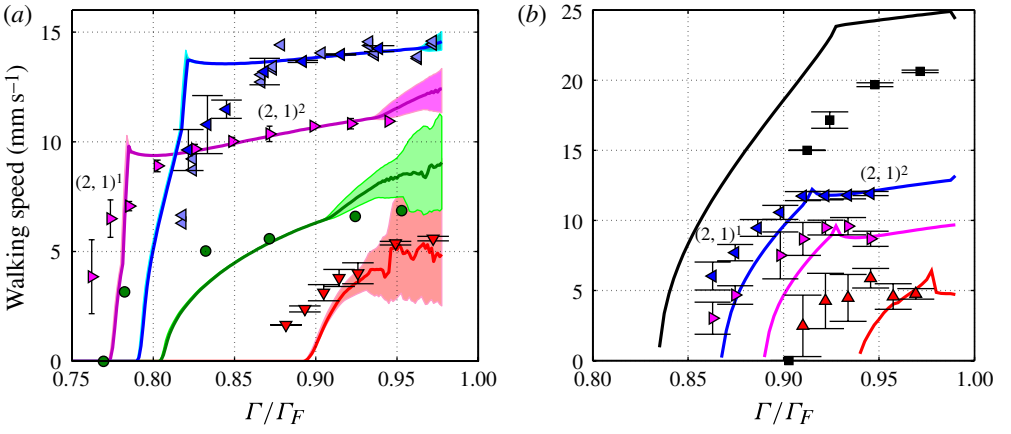

FIGURE 12. (Colour online) The walking speeds of silicone oil droplets for (*a*) $\nu = 20$ cSt at $f = 80$ Hz and (*b*) $\nu = 50$ cSt at $f = 50$ Hz, as a function of the dimensionless driving acceleration. Our model predictions (lines) are compared to the existing data for selected drop radii. These are: (*a*) $R_0 = 0.31$ mm (▼), 0.35 mm (◯), 0.38 mm (►) and 0.40 mm (◄, ◁); (*b*) $R_0 = 0.25$ mm (▲), 0.34 mm (►), 0.39 mm (◄) and 0.51 mm (■). In panel (*a*), the predicted range of instantaneous walking speeds in the chaotic bouncing regime is indicated by the shaded regions. Discontinuities in slope of the theoretical curves indicate a switching of vertical bouncing modes from $(2, 1)^1$ to $(2, 1)^2$ with increasing Γ. Characteristic error bars are shown.

Our model predicts that, in most walking regions, the droplet is in the higher-energy $(2, 1)^2$ bouncing mode (see figures 3*b* and 16*b*), especially for higher frequencies, smaller drops and lower viscosities. However, there are cases (e.g. when $\nu = 50$ cSt and $f = 50$ Hz) when the model predicts that drops can walk even in the lower-energy $(2, 1)^1$ mode (see figures 3*a* and 16*a*). We note that our model is less accurate for the lower-energy mode, due to its longer average contact time, which leads to an overestimation of the walking regime for $\nu = 50$ cSt and $f = 50$ Hz.

In figure 12, we compare our model predictions of the walking speeds with the existing and new experimental data. As with the walking thresholds, the match is better for fluids with smaller viscosity. Compared to the previous predictions for the walking speeds (Protière *et al.* 2006), which were significantly too high, our model achieves a satisfactory match. We note that a slight overestimate for larger drops (see figure 12*b*, $R_0 = 0.51$ mm) arises as a result of the point force approximation (equation (A 27)). The walking speed generally increases with increasing driving acceleration and drop size. However, this trend can be violated when the drop switches from one bouncing mode to another. Most striking is the switch from the $(2, 1)^1$ mode to $(2, 1)^2$, as is evidenced by the discontinuities in the theoretical curves in figure 12(*b*) in the region $0.9 < \Gamma/\Gamma_F < 0.95$ for the smallest three drops examined. When walking occurs in the region of chaotic vertical motion, the walking speed varies between each contact depending on the phase and depth of the previous impact. This is indicated in figure 12(*a*) for the three smallest drops by the shaded regions, which mark the possible range of the instantaneous walking speeds. The solid curves within these shaded regions were obtained by averaging the horizontal speed over many impacts.

In order to verify that the switching between the two different (2, 1) modes is not a peculiarity of our theoretical model, we measured the contact time of drops in or

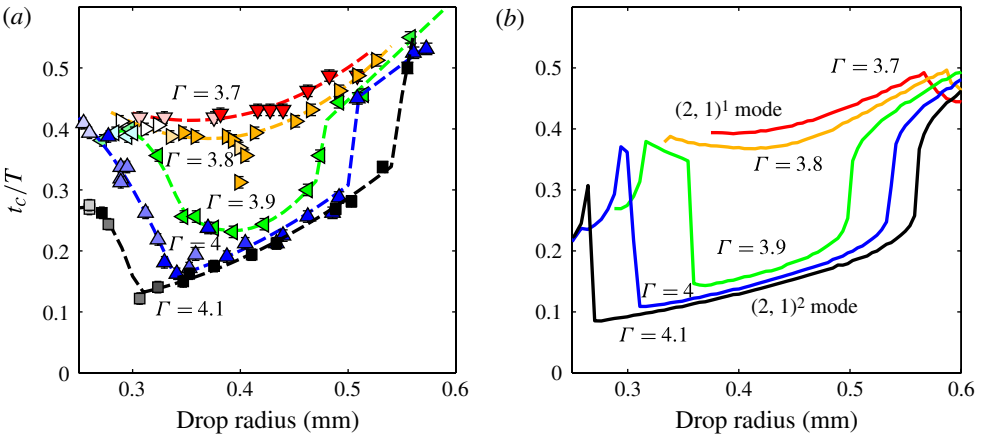

FIGURE 13. (Colour online) The relative contact time t_c/T (the fraction of the drop's bouncing period T spent in contact with the bath), as a function of the drop radius. (*a*) Experimental results for dimensionless driving $\Gamma = 3.7$ (▼), 3.8 (►), 3.9 (◄), 4.0 (▲) and 4.1 (■) are compared to (*b*) theoretical predictions for the same set of Γ. The appearance of the higher-energy $(2, 1)^2$ mode (see figure 3*a*,*b*) at $\Gamma = 3.9$ is marked by a discrete decrease of contact time.

near the walking regime. The ratio of the contact time to the period of vertical motion, t_c/T, is shown as a function of drop radius in figure 13. The experimental results are shown in figure 13(*a*), while the theoretical predictions are shown in figure 13(*b*). Both plots indicate the appearance of the $(2, 1)^2$ mode at $\Gamma = 3.9$, which is characterized by $t_c/T < 0.3$. Also evident is the increased range of drops in the $(2, 1)^2$ mode with increased driving acceleration. We observe a satisfactory match between theory and experiments. The model consistently underestimates the contact times relative to the experiments, owing to the different way of defining contact in each case. Experimentally, we measured the interval between the first contact and detachment of the drop. This interval is in general longer than the period of positive reaction force, our theoretical definition of contact time, due to the effects of the intervening air layer dynamics.

Figure 14 shows the dependence of the walking speed on the driving acceleration and drop size, as predicted by our model. The maximum walking speeds arise at the Faraday threshold for drops near the upper limit of the walking regime. In figure 14(*a*), the region of chaotic vertical motion ($0.4 < \Omega < 0.7$, and $0.9 < \Gamma/\Gamma_F < 1$) is marked by oscillations in the walking speeds. In figure 14(*b*), the transition from the $(2, 1)^1$ mode to the $(2, 1)^2$ mode can be discerned from the sharp change in orientation of the velocity isoclines.

In figure 15(*a*,*c*), we show the extent and depth $1 - \Gamma_W/\Gamma_F$ of the walking region across a range of driving frequencies, as predicted using a single value for the proportionality constant $C = 0.2$. Our model predicts that walking only occurs for 52 Hz $\leqslant f \leqslant$ 103 Hz when $\nu = 20$ cSt and for 39 Hz $\leqslant f \leqslant$ 80 Hz when $\nu = 50$ cSt, which is in agreement with the range found experimentally by Protière *et al.* (2005) (see table 2). In figure 15(*b*,*d*) we show the different vertical bouncing modes of drops at the walking threshold. Besides the familiar (2, 1) modes and their period-doubled variants (arising for $f \geqslant 70$ Hz for $\nu = 20$ cSt, and for $f \geqslant 50$ Hz for $\nu = 50$ cSt), we

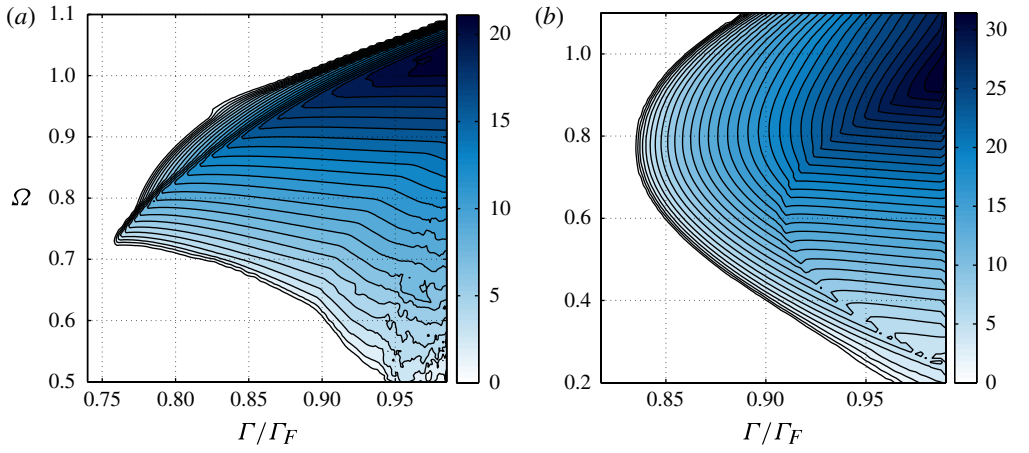

FIGURE 14. (Colour online) The walking speeds (mm s^{-1}) obtained with our model for (*a*) $\nu = 20$ cSt at $f = 80$ Hz and (*b*) $\nu = 50$ cSt at $f = 50$ Hz. The horizontal axis indicates the ratio of the peak driving acceleration to the Faraday threshold, while the vertical axis indicates the vibration number $\Omega = \omega/\omega_D$.

also note the existence of 'limping' drops at smaller frequencies, for which two strong impacts of the drop, roughly one Faraday period apart, are separated by a relatively weak impact. A few of the simplest limping modes are shown in figure 16(*d–f*), together with chaotic limping (figure 16*g*) and non-limping modes (figure 16*a–c*). Finally, we note that the lower boundary of the walking region consists predominantly of chaotic walkers, for which the vertical motion is aperiodic. This makes it difficult to experimentally determine the walking threshold for small drops, for which random horizontal motion might also be attributable to weak air currents above the bath.

6. Conclusion

Several new phenomena have been observed experimentally and rationalized theoretically, most notably the coexistence of different vertical bouncing modes in the walking regime for identical system parameters. Switching between the different modes can lead to discontinuous or non-monotonic dependence of the walking speed and contact time on the driving acceleration. Our model also predicts that, for higher frequencies, the walking regime does not necessarily extend to the Faraday threshold, and may instead give way to a chaotic walking state.

We have combined models for the vertical and horizontal dynamics of bouncing drops in order to rationalize the extent of the walking regimes and the dependence of walking speeds on the forcing acceleration. We have reduced the number of free parameters from as many as five in some of the previous models to one with tight bounds. Our remaining fitting parameter is the constant of proportionality C, defined in (4.1), which can be rewritten

$$C = \frac{\int F^T(\tau)\,\mathrm{d}\tau}{\int F^N(\tau)X_\tau\,\mathrm{d}\tau} = \frac{\int X_{\tau\tau}\,\mathrm{d}\tau}{\int X_\tau(Z_{\tau\tau} + Bo^*(\tau))\,\mathrm{d}\tau} \approx \frac{1 - C_R^T}{(1 + C_R^N)We_{in}^{1/2}}, \tag{6.1}$$

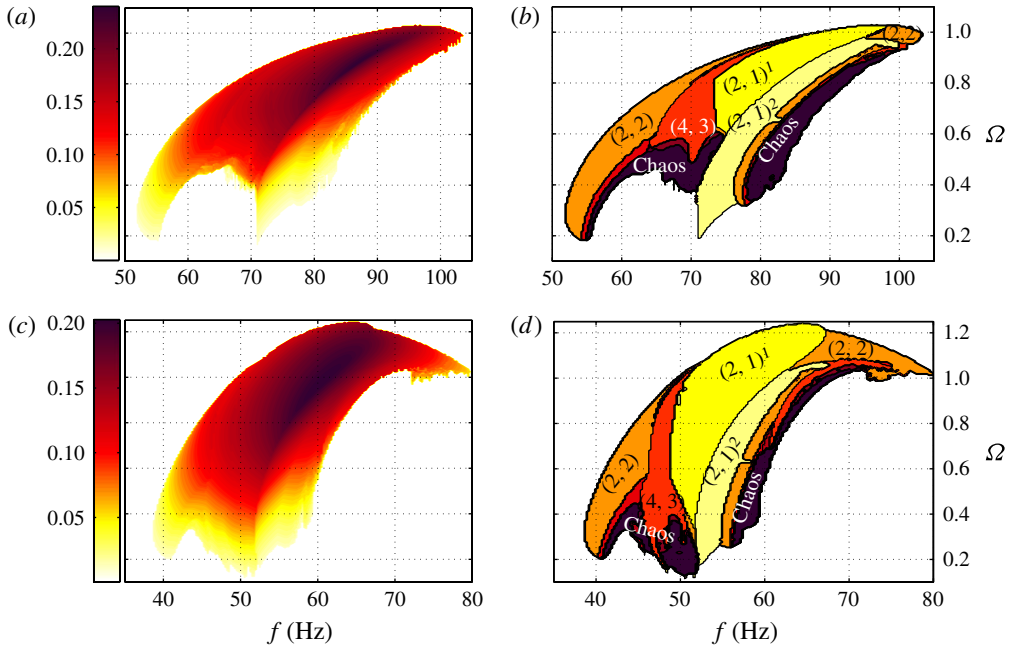

FIGURE 15. (Colour online) The walking region for (*a*,*b*) 20 cSt and (*c*,*d*) 50 cSt silicone oil drops, as predicted by our model (equations (4.6)–(4.10)). Horizontal axes indicate the driving frequency f, while the vertical axes indicate $\Omega = \omega/\omega_D$. In panels (*a*,*c*), the relative distance from walking threshold to Faraday threshold $1 - \Gamma_W/\Gamma_F$ is shown. The various modes of vertical bouncing at the walking threshold are shown in panels (*b*,*d*), the most significant of which are the two (2, 1) modes (resonant bouncing with the Faraday period, see figure 16*a*,*b*), and the different kinds of 'limping' drops (the (2, 2), (4, 3) and (4, 4) modes, figure 16*d*–*f*), where a relatively weak contact arises between a pair of strong contacts. In general, the walking regime's lower boundary adjoins a region marked by chaotic bouncing (figure 16*c*,*g*).

where F^N and F^T are the normal and tangential components of the dimensionless reaction force acting on the drop during contact, and C_R^N and C_R^T are the normal and tangential coefficients of restitution, respectively. The values of C used in our model were between 0.17 and 0.33, while experimentally it was found to be near 0.3. The match with experiments is improved significantly relative to existing models (Couder *et al.* 2005*b*; Protière *et al.* 2006) as a result of a more thorough analysis of the standing waves created by the drop impacts and the forces acting on the drop during impact.

Our model, summarized in § 4.4, combines the description of the vertical dynamics (4.6) developed in MBI and the horizontal dynamics (4.10) via an approximate description of the Faraday wave field (4.7)–(4.9). The approximation, derived analytically in the Appendix, is valid for a finite range of oil viscosities defined in (A 51), which includes those examined experimentally. Assuming that the drop is a resonant walker in the $(2, 1)^2$ bouncing mode and that its horizontal speed changes slowly relative to its bouncing period, one can average out the vertical motion and derive a trajectory equation (4.16) for the drop's horizontal motion. The more exotic walking states, such as limping or chaotic walking, will be the subject of a future study of gait changes in walking droplets (Wind-Willassen *et al.* 2013).

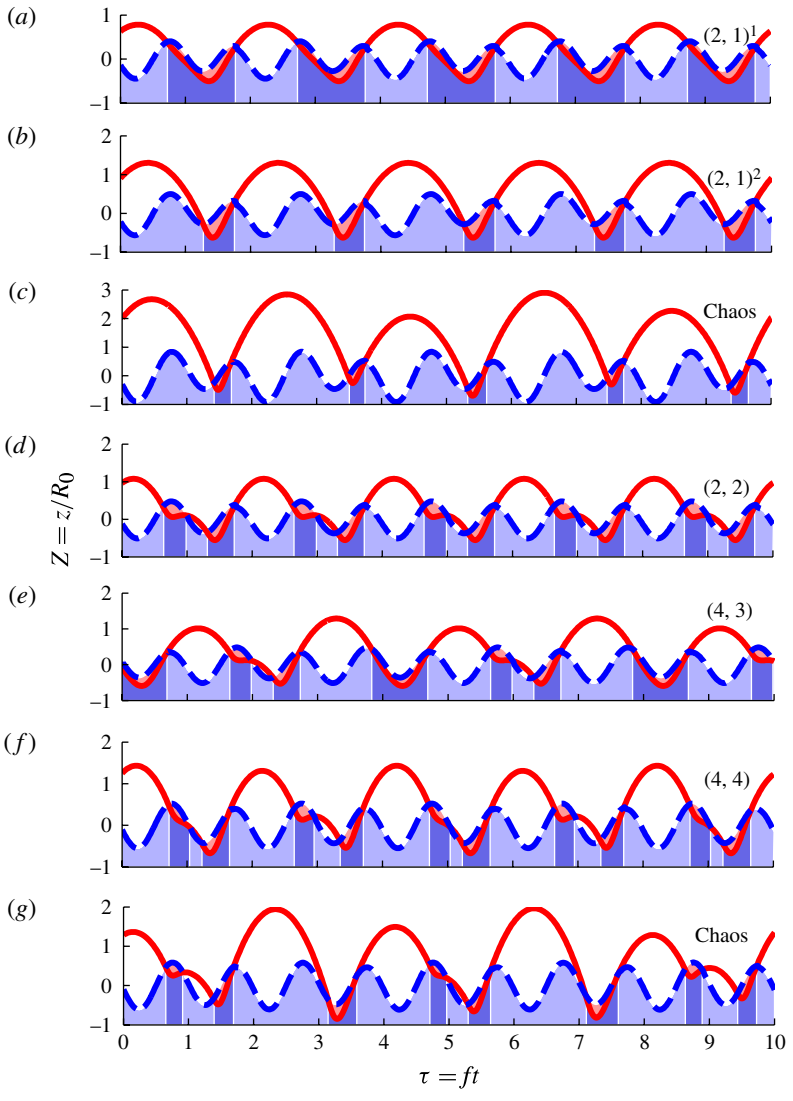

FIGURE 16. (Colour online) The most common bouncing modes of 20 cSt drops near the walking threshold: (*a*) the $(2, 1)^1$ mode, for $f = 80$, $\Omega = 0.8$, $\Gamma = 3.36$; (*b*) the $(2, 1)^2$ mode, for $f = 80$, $\Omega = 0.7$, $\Gamma = 3.55$; (*c*) chaotic bouncing, for $f = 80$, $\Omega = 0.4$, $\Gamma = 4.14$; (*d*) the $(2, 2)$ mode, for $f = 60$, $\Omega = 0.6$, $\Gamma = 2.3$; (*e*) the $(4, 3)$ mode, for $f = 70$, $\Omega = 0.6$, $\Gamma = 2.87$; (*f*) the $(4, 4)$ mode for $f = 62$, $\Omega = 0.51$, $\Gamma = 2.43$; and (*g*) chaotic limping for $f = 70$, $\Omega = 0.45$, $\Gamma = 2.99$. The modes in panels (*d–g*) are referred to as 'limping' modes, due to the short steps alternating with long ones.

The model was kept relatively simple for the sake of tractability. As a result, there are cases where the simplifying assumptions are being pushed to their limits; nevertheless, it should be straightforward to extend the validity of our model starting from the same equations and include higher-order corrections. The first of the simplifications made was the approximation of the underlying standing-wave field by the formula (3.7), which works well for the oil viscosities used in our experiments,

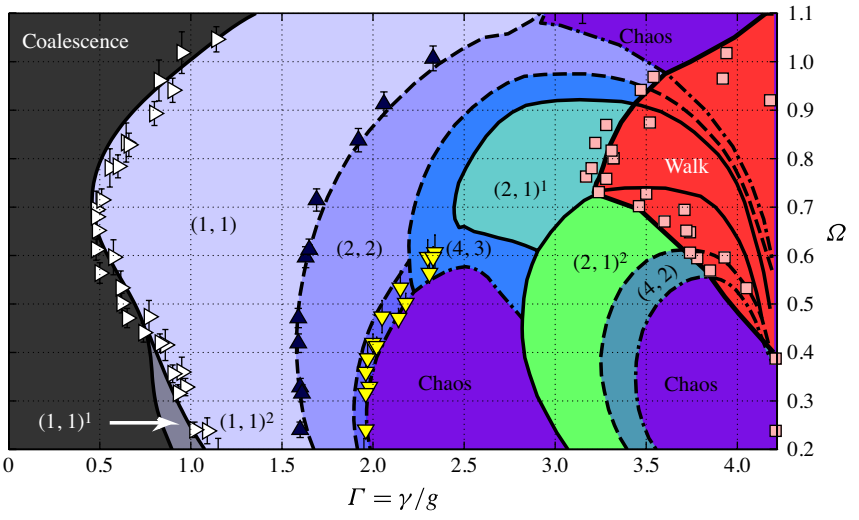

FIGURE 17. (Colour online) Comparison of the regime diagram for 20 cSt silicone oil and $f = 80$ Hz, as predicted by our model, to the experimental data. The data on the bouncing threshold (►), first (▲) and second (▼) period doubling and on the walking threshold (■) are shown. The rightmost boundary corresponds to the Faraday threshold Γ_F.

as shown in figure 6. However, if the model is to be extended to smaller or higher viscosities, it might be necessary to including higher-order terms in evaluating the integral (A 47) using Laplace's method, in order to achieve sufficient accuracy within the first few Faraday periods. The heuristic formula for the tangential force during impact is another major simplification of the model, which ties the tangential and normal components of the reaction force. The actual temporal profile of the tangential force is likely to be slightly different from that given by (A 46), leading to increased error for long contact time. On the other hand, when the contact time is much shorter than the Faraday period, the temporal profile is inconsequential, as only the overall loss of tangential momentum will affect the walking dynamics.

More important, and likely the major source of error in our model, is the approximation of the horizontal kick received by the drop during impact, as summarized in (4.5). This result was deduced by assuming that the impact is much shorter than the Faraday period and that the bath disturbance radius is much shorter than the Faraday wavelength. For larger drops or drops in lower-energy modes, these assumptions are no longer strictly valid. Nevertheless, the model predictions still fare rather well. In order to improve upon this approximation, terms involving higher spatial and temporal derivatives of the surface profile could be added to (4.5). On its own (Oza, Rosales & Bush 2013), or combined with a numerical model that captures the outgoing transient surface wave created at each impact, our model represents the first rational hydrodynamic pilot-wave theory, and provides a solid foundation for modelling the quantum-like behaviour of walking droplets.

Acknowledgements

The authors thank D. Harris for his tireless assistance with the experimental side of this paper and Y. Couder and his coworkers for valuable discussions. The authors

gratefully acknowledge the generous financial support of the NSF through grant CBET-0966452 and the MIT–France Program.

Appendix. Derivation of the equations for the bath interface shape

We here derive the equations governing the evolution of the radially symmetric disturbance on a liquid bath caused by the rebound of a liquid drop. Besides the assumption of radial symmetry, we approximate the excess pressure distribution (the difference between the local pressure and the atmospheric pressure) over the contact area between the drop and the bath (i.e. the area where the intervening air layer thickness is much smaller than the drop radius and the two liquid–air surfaces have almost the same profile) by a constant: $p(r, t) = p(t)$. Non-dimensionalizing using the drop radius R_0 and the characteristic drop oscillation frequency $\omega_D = (\sigma/\rho R_0^3)^{1/2}$, we have

$$h = h'/R_0, \quad r = r'/R_0, \quad \tau = t\omega_D, \quad Z = z/R_0, \quad k = k'R_0, \tag{A 1}$$

where $h = h(r, \tau)$ is the bath surface height, r the distance from the axis of symmetry, τ the dimensionless time, Z the drop vertical height and k the dimensionless wavenumber. Then the extra surface potential energy is given by

$$\Delta\mathscr{S}\mathscr{E} = \sigma R_0^2 \int_0^\infty 2\pi r[\sqrt{1 + h'^2(r)} - 1]\,\mathrm{d}r \approx \pi\sigma R_0^2 \int_0^\infty r h'^2(r)\,\mathrm{d}r, \tag{A 2}$$

provided that $h'(r) \ll 1$, where σ is the liquid surface tension. Similarly, the extra gravitational energy is given by

$$\Delta\mathscr{P}\mathscr{E} = \rho g R_0^4 \int_0^\infty 2\pi r \frac{1}{2} h^2(r)\,\mathrm{d}r = \pi\rho g R_0^4 \int_0^\infty r h^2(r)\,\mathrm{d}r, \tag{A 3}$$

where ρ is the liquid density and g the gravitational acceleration. Finally, the presence of the excess pressure above the contact area gives rise to a pressure potential energy

$$\Delta\mathscr{P}\mathscr{E}_P = p(\tau) R_0^3 \int_0^w 2\pi r h(r)\,\mathrm{d}r = 2\pi R_0^3 p(\tau) \int_0^w r h(r)\,\mathrm{d}r, \tag{A 4}$$

where w is the dimensionless radius of the contact area. In order to proceed further, we need to convert the equations derived so far into ones involving the Hankel transform of the surface height. The Hankel transform $H(k)$ of the surface height $h(r)$ is defined as

$$H(k) = \int_0^\infty h(r) \mathrm{J}_0(kr) r\,\mathrm{d}r \quad \text{so that} \quad h(r) = \int_0^\infty H(k) \mathrm{J}_0(kr) k\,\mathrm{d}k, \tag{A 5}$$

where $\mathrm{J}_0(x)$ is the Bessel function of the first kind of order zero. The Plancherel theorem states that, for two functions $f(r)$ and $g(r)$ and their Hankel transforms $F(k)$ and $G(k)$, the following relationship holds:

$$\int_0^\infty f(r) g(r) r\,\mathrm{d}r = \int_0^\infty F(k) G(k) k\,\mathrm{d}k. \tag{A 6}$$

Using the Plancherel theorem, we can easily convert (A 3) to

$$\Delta\mathscr{P}\mathscr{E} = \pi g R_0^4 \int_0^\infty H^2(k) k\,\mathrm{d}k. \tag{A 7}$$

Substituting for $h'(r) = -\int k^2 \mathrm{J}_1(kr) H(k)\,\mathrm{d}k$ into (A 2) and using the closure equation $\int_0^\infty x \mathrm{J}_i(ux)\mathrm{J}_i(vx)\,\mathrm{d}x = \delta(u-v)/u$, where $\delta(x)$ is the Dirac delta function, we obtain

$$\Delta\mathscr{S}\mathscr{E} = \pi\sigma R_0^2 \int_0^\infty H^2(k) k^3\,\mathrm{d}k. \tag{A 8}$$

Finally, (A 4) can be rewritten as

$$\begin{aligned}\Delta\mathscr{P}\mathscr{E}_P &= 2\pi R_0^3 p(\tau) \int_0^\infty H(k) k \int_0^w \mathrm{J}_0(kr) r\,\mathrm{d}r\,\mathrm{d}k \\ &= 2\pi R_0^3 p(\tau) \int_0^\infty H(k)\mathrm{J}_1(kw) w\,\mathrm{d}k.\end{aligned} \tag{A 9}$$

A.1. *Small viscosity*

When the viscosity of the liquid is small, we can approximate the flow inside the bath by potential flow. The general axisymmetric solution to $\nabla^2\Phi = 0$ in cylindrical coordinates, which decays as $r \to \infty$, can be written as

$$\Phi(r, z, t) = \int_0^\infty \varphi(k, \tau)\mathrm{J}_0(kr)\mathrm{e}^{kz} k\,\mathrm{d}k. \tag{A 10}$$

The linearized kinematic boundary condition at the surface $R_0\,\partial h(r,t)/\partial t = u_z(x, 0, t) = (1/R_0)\,\partial\Phi/\partial z|_{z=0}$ implies

$$R_0^2 \int_0^\infty \dot{H}(k, t)\mathrm{J}_0(kx) k\,\mathrm{d}k = \int_0^\infty \varphi(k, t)\mathrm{J}_0(kx) k^2\,\mathrm{d}k, \tag{A 11}$$

and therefore $\varphi(k, t) = R_0^2\dot{H}(k, t)/k$. Equation (A 10) can therefore be written as

$$\Phi(r, z, \tau) = R_0^2 \int_0^\infty \dot{H}(k, \tau)\mathrm{J}_0(kx)\mathrm{e}^{kz}\,\mathrm{d}k. \tag{A 12}$$

The kinetic energy of the bath is given by

$$\begin{aligned}\frac{\mathscr{K}\mathscr{E}}{\rho} &= \frac{1}{2}\int_V \boldsymbol{\nabla}\Phi\cdot\boldsymbol{\nabla}\Phi\,\mathrm{d}V = \frac{1}{2}\int_V \boldsymbol{\nabla}\cdot(\Phi\boldsymbol{\nabla}\Phi)\,\mathrm{d}V \\ &= \frac{1}{2}\int_S \Phi\boldsymbol{\nabla}\Phi\cdot\mathrm{d}\mathbf{S} = \frac{R_0}{2}\int_0^\infty \Phi\frac{\partial\Phi}{\partial z} 2\pi x\,\mathrm{d}x = \pi R_0^5 \int_0^\infty \dot{H}^2(k, t)\,\mathrm{d}k,\end{aligned} \tag{A 13}$$

where we have used the Plancherel theorem again and approximated the direction of the surface normal vector as vertical. It can similarly be shown that the viscous dissipation in the bath is given by

$$\mathscr{D} = 8\pi\mu R_0^3 \int_0^\infty \dot{H}^2(k, t) k^2\,\mathrm{d}k. \tag{A 14}$$

Then the equations of motion can be derived via the Euler–Lagrange equation with dissipation (Flügge 1959; Torby 1984, p. 271)

$$\frac{\mathrm{d}}{\mathrm{d}t}\frac{\partial\mathfrak{L}}{\partial\dot{H}} + \frac{1}{2}\frac{\partial\mathscr{D}}{\partial\dot{H}} = \frac{\partial\mathfrak{L}}{\partial H}, \tag{A 15}$$

where $\mathfrak{L}$ is the Lagrangian, defined as

$$\mathfrak{L} = \mathscr{K}\mathscr{E} - \Delta\mathscr{S}\mathscr{E} - \Delta\mathscr{P}\mathscr{E} - \mathscr{P}\mathscr{E}_P. \tag{A 16}$$

Substituting for $\mathfrak{L}$ from (A 16) into (A 15), and using the expressions (A 7)–(A 9), (A 13) and (A 14) yields

$$\ddot{H} + 2\frac{\mu k^2}{\rho R_0^2}\dot{H} + \frac{\sigma}{\rho R_0^3}[k^3 + kBo]H + \frac{pw}{\sigma R_0^2}\mathrm{J}_1(kw) = 0, \tag{A 17}$$

where $Bo = \rho g R_0^2/\sigma$ is the Bond number. Going back to the dimensionless time $\tau = t\omega_D$, we obtain

$$H_{\tau\tau} + 2Ohk^2 H_\tau + [k^3 + kBo]H + \frac{R_0 pw}{\sigma}\mathrm{J}_1(kw) = 0, \tag{A 18}$$

with $Oh = \mu/(\sigma\rho R_0)^{1/2}$ being the Ohnesorge number. The total reaction force F_R acting on the bath, given by $F_R = R_0^2 \int_0^w 2\pi rp\,\mathrm{d}r = \pi w^2 R_0^2 p$, is the same as the force acting on the drop, so that $m\ddot{z} = F_R - mg$. Rewriting the last expression in terms of the dimensionless coordinates, we get $Z_{\tau\tau} = \frac{3}{4}R_0 w^2 p/\sigma - Bo \equiv F - Bo$, and so (A 18) can be rewritten as

$$H_{\tau\tau} + 2Ohk^2 H_\tau + [k^3 + kBo]H + \frac{4}{3}F\frac{\mathrm{J}_1(kw)}{w} = 0 \quad \text{with } F = Z_{\tau\tau} + Bo. \tag{A 19}$$

A.2. *Appreciable viscosity*

For appreciable viscosity, the fluid motion diverges significantly from potential flow near the surface, and the method described above can no longer be applied. However, considerable accuracy can be maintained without sacrificing the simplicity of (A 19) by replacing Oh by a phenomenological or 'effective' Ohnesorge number Oh_e, so that the rates of decay predicted by this pseudo-linear model and the full analytic model coincide. Alternatively, one can try to match the experimentally observed decay rates, as was done by Eddi *et al.* (2011). To determine the value of Oh_e analytically, we follow Prosperetti (1976) and match the principal decay rates of the surface waves with wavelength k by replacing (A 19) with

$$A(k, Oh, Bo)H_{\tau\tau} + 2OhD(k, Oh, Bo)k^2 H_\tau + [k^3 + kBo]H + \frac{4}{3}F\frac{\mathrm{J}_1(kw)}{w} = 0, \tag{A 20}$$

where the coefficients A and D are chosen so that the roots of the equation

$$Ax^2 + 2aDx + 1 = 0, \quad \text{where } a = \frac{Ohk^{3/2}}{(Bo + k^2)^{1/2}}, \tag{A 21}$$

are the two roots with the largest real part of the polynomial equation

$$[(x + 2a)^2 + 1]^2 = 16a^3(x + a). \tag{A 22}$$

Then

$$Oh_e = OhD. \tag{A 23}$$

It can be shown that $D \to 2$ as $\mu \to 0$, while $D \to 1$ as $\mu \to \infty$ (Lamb 1932). On the other hand, $A \to 1$ as $\mu \to 0$ and remains close to 1 for $Ohk^{1/2} < 0.3$. From now on we will thus approximate A by 1 and write Oh_e instead of Oh.

When the bath is shaken vertically with frequency f and peak acceleration Γg, we need only replace Bo by an effective Bond number Bo^*, which is now a function of time,

$$Bo^*(\tau) = Bo(1 + \Gamma \sin \Omega\tau), \tag{A 24}$$

and represents the sum of gravity and fictitious forces in the non-inertial frame of reference fixed with the oscillating bath. Here $\Omega = \omega/\omega_D = 2\pi f/\omega_D$ is the vibration number. Thus we arrive at the equation

$$H_{\tau\tau} + 2Oh_e k^2 H_\tau + [k^3 + kBo^*(\tau)]H = -\frac{4}{3}F\frac{\mathrm{J}_1(wk)}{w}. \tag{A 25}$$

We are interested in the behaviour of the model for k near k_F, the Faraday wavelength, which is defined by the dimensionless dispersion relation (see Kumar 1996, p. 1121)

$$k_F^3 + Bok_F = \tfrac{1}{4}\Omega^2, \tag{A 26}$$

particularly in the regime $\Omega \lesssim 1$ where we observe walking. Since Bok_F is positive, we have $k_F \leqslant (\Omega/2)^{2/3}$.

A.3. *Point force approximation*

We seek to show that, for the range of parameters explored in our experiments, wk_F is always small, so we can approximate the impact forcing by a point forcing. During rebound, the extra pressure in the intervening air layer beneath the contact area can be bounded below by half the capillary pressure σ/R_0 (Hartland 1971). The drop's change of momentum during impact is at most $\Delta P \approx \frac{4}{3}\pi\rho R_0^3 2v$, where v is the drop speed at impact. The rebound time is roughly $t_C \approx 4(\rho R_0^3/\sigma)^{1/2}$ (see MBI, figure 8); thus, the typical force on the drop during rebound is $F_R \approx \Delta P/t_C \approx (\rho R_0^3\sigma)^{1/2}2v$. Dividing the typical reaction force by the lower bound on the pressure yields an upper bound on the typical contact area: $\pi R_0^2 w^2 \leqslant 2R_0^2 We^{1/2}$, where $We = \rho R_0 v^2/\sigma$ is the Weber number. Hence $w^2 \leqslant 2We^{1/2}/\pi$. For droplets bouncing periodically with the Faraday period (twice the driving period), we have $Z(\tau + (4\pi/\Omega)) = Z(\tau)$. The acceleration of the drop in flight is Bo, so the maximum dimensionless relative velocity is $We_{max}^{1/2} = Bo(2\pi/\Omega)$. Therefore, $wk_F \leqslant [Bo(2\pi/\Omega)(2/\pi)]^{1/2}(\Omega/2)^{2/3} = (Bo)^{1/2}(\Omega/2)^{1/6}$.

Since $\mathrm{J}_1(x) = (x/2) - (x^3/16) + O(x^5)$, for $x^2/8 \ll 1$ we can approximate $\mathrm{J}_1(x)$ by $x/2$. Thus we can write $\mathrm{J}_1(wk)/w = k/2$, provided $w^2k_F^2/8 \leqslant 2Bo(\Omega/2)^{1/3} \ll 1$. Restricting ourselves to the region $\Omega \leqslant 1$, it follows that by using the point force approximation we commit a relative error of at most $2Bo$ in estimating the forcing for each wavenumber. Typically, $R_0 \approx 0.3$–0.4 mm ($Bo = 0.04$–0.08), leading to a relative error of at most 10–15 %. We note that this is likely to be an overestimate of the relative error, as the actual contact area and relative velocity of impact will both be significantly smaller than the upper bounds used.

A.4. *Analysis of the standing waves for small viscosity*

We shall henceforth use the point force approximation, bearing in mind that it might lead to an overestimate of the bath deformation for larger drops ($R_0 > 0.4$ mm). Thus (A 26) simplifies to

$$H_{\tau\tau} + 2Oh_e k^2 H_\tau + H(k^3 + kBo^*(\tau)) = -\tfrac{2}{3}kF(\tau). \tag{A 27}$$

We shall write $\Upsilon(k) = Oh_e(k)k^2$ for simplicity and consider presently the case of no forcing (right-hand side of (A 27) equals zero), assuming $Oh_e \ll 1$:

$$H_{\tau\tau} + 2\Upsilon H_\tau + H(k^3 + kBo^*(\tau)) = 0. \tag{A 28}$$

Making the substitution $H(\tau) = \exp(-\Upsilon\tau)\mathscr{H}(\tau)$, we can convert (A 28) into the Mathieu equation, and by applying Floquet's theorem we obtain the form of general

solution of (A 28):

$$H(\tau) = c_1 H_1(\tau) + c_2 H_2(\tau)$$
$$= c_1 \exp(\beta\tau)\bar{H}(\tau) + c_2 \exp[(\beta - 2\Upsilon)\tau]\bar{H}(\pi/\Omega - \tau), \tag{A 29}$$

where $\bar{H}(\tau)$ is a periodic function with period $4\pi/\Omega$. Below the Faraday threshold, we may assume without loss of generality that $\beta < \Upsilon < 0$, so that $H_2(\tau)$ decays faster than $H_1(\tau)$. Thus, for large times, $H_1(\tau)$ will dominate the behaviour of $H(\tau)$. Now we return to (A 27) and consider the Green's function $G(\tau, \tau_0)$ for the forcing, defined as the solution of

$$G_{\tau\tau} + 2\Upsilon G_\tau + G(k^3 + kBo(1 + \Gamma \sin \Omega\tau)) = \delta(\tau - \tau_0). \tag{A 30}$$

We can write $G(\tau, \tau_0)$ as a linear combination of the two solutions of the homogeneous problem (A 28). Equation (A 30) implies that $G(\tau_0, \tau_0) = 0$ and $G_\tau(\tau_0^+, \tau_0) = 1$, from which we derive

$$G(\tau, \tau_0) = \frac{H_1(\tau)H_2(\tau_0) - H_2(\tau)H_1(\tau_0)}{H_{1\tau}(\tau_0)H_2(\tau_0) - H_1(\tau_0)H_{2\tau}(\tau_0)}. \tag{A 31}$$

The denominator in (A 31) is the Wronskian $W(H_2, H_1)(\tau_0)$, which satisfies $W_\tau = -\Upsilon W$, implying $W(\tau_0) = \exp(-\Upsilon\tau_0)W(0)$. Using this identity and the forms of H_1 and H_2, we can express (A 31) as

$$G(\tau, \tau_0) = \frac{\mathrm{e}^{-\beta(\tau-\tau_0)}\bar{H}(\tau)\bar{H}\left(\frac{\pi}{\Omega} - \tau_0\right) - \mathrm{e}^{(\beta-2\Upsilon)(\tau-\tau_0)}\bar{H}(\tau_0)\bar{H}\left(\frac{\pi}{\Omega} - \tau\right)}{\bar{H}_\tau(0)\bar{H}\left(\frac{\pi}{\Omega}\right) + \bar{H}(0)\bar{H}_\tau\left(\frac{\pi}{\Omega}\right) - 2\bar{H}(0)\bar{H}\left(\frac{\pi}{\Omega}\right)(\beta - \Upsilon)}. \tag{A 32}$$

By neglecting the H_2 component of $G(\tau, \tau_0)$ for large times, when it has decayed sufficiently relative to H_1, we can approximate the solution to (A 27) as follows:

$$H(\tau) \approx \left[\int -\frac{2}{3}kF(\tau')G_1(\tau')\,\mathrm{d}\tau'\right]\mathrm{e}^{-\beta\tau}\bar{H}(\tau),$$

$$\text{where } G_1(u) = \frac{\exp(\beta u)\bar{H}\left(\frac{\pi}{\Omega} - u\right)}{\bar{H}_\tau(0)\bar{H}\left(\frac{\pi}{\Omega}\right) + \bar{H}(0)\bar{H}_\tau\left(\frac{\pi}{\Omega}\right) + 2(\Upsilon - \beta)\bar{H}(0)\bar{H}\left(\frac{\pi}{\Omega}\right)}. \tag{A 33}$$

In order to proceed, we need to determine the periodic function $\bar{H}(\tau)$. We decompose $\bar{H}(\tau)$ into its Fourier components, starting with the sub-harmonic component with angular frequency $\Omega/2$:

$$H(\tau) = \mathrm{e}^{\beta\tau}\sum_{n=-\infty}^{\infty}\hat{H}_n\mathrm{e}^{\mathrm{i}\Omega(n/2)\tau}. \tag{A 34}$$

Substituting this form into (A 28) yields

$$\hat{H}_n\left[k^3 + kBo - \frac{n^2}{4}\Omega^2 + 2\Upsilon\beta + \beta^2 + \mathrm{i}(\beta\Omega n + \Upsilon\Omega n)\right]$$
$$- \frac{\mathrm{i}}{2}kBo\Gamma[\hat{H}_{n-2} - \hat{H}_{n+2}] = 0. \tag{A 35}$$

This recurrence relation along with the reality condition $\hat{H}_n = \hat{H}^*_{-n}$ and smoothness of $H(t)$, $\lim_{|n|\to\infty}|n\hat{H}_n| = 0$, allows one to obtain the complete Fourier series of $\bar{H}(\tau)$,

involving two multiplicative constants (one for the odd terms, the other for the even terms), which are determined from the initial conditions. The growth rate β depends on Γ, corresponding to the amplitude of the bath oscillation; for $\Gamma < \Gamma_F$, $\beta < 0$ and $H(\tau)$ decays exponentially in time; while for $\Gamma > \Gamma_F$, $\beta > 0$ and $H(\tau)$ grows exponentially. Here Γ_F denotes the Faraday threshold, and we will be interested in the behaviour of $H(\tau)$ for Γ near Γ_F. Since $\beta = 0$ for $\Gamma = \Gamma_F$, β must be small for Γ near Γ_F. Finally, the value of the Faraday threshold depends strongly on the wavenumber k. We are interested in the wavenumbers k near k_C, the critical wavenumber where $\Gamma_F(k)$ achieves a global minimum. Assuming that for small damping ($Oh_e \ll 1$) the function $H(\tau)$ is nearly sinusoidal, so that the terms $\hat{H}_{\pm 1}$ dominate all others, we obtain

$$\hat{H}_1 \left[k^3 + kBo - \frac{\Omega^2}{4} + 2\Upsilon\beta + \mathrm{i}(\beta\Omega + \Upsilon\Omega) \right] - \frac{\mathrm{i}}{2} kBo\Gamma \hat{H}_1^* = 0. \tag{A 36}$$

Writing $\hat{H}_1 = |\hat{H}_1| \mathrm{e}^{i\theta}$ and considering the real and imaginary parts separately, we obtain

$$k^3 + kBo - \tfrac{1}{4}\Omega^2 + 2\Upsilon\beta = \tfrac{1}{2} kBo\Gamma \sin(2\theta), \quad \beta\Omega + \Upsilon\Omega = \tfrac{1}{2} kBo\Gamma \cos(2\theta). \tag{A 37}$$

When $Oh_e = 0$, $\Gamma_F = 0$ and $k_C = k_F$; therefore, we expect $k_C \approx k_F$ when Oh_e is small. Then, we assume $|\beta| \ll 1$, write $k = k_F(1 + \delta k)$ with $\delta k \ll 1$, and expand in powers of δk to obtain

$$\frac{\sin 2\theta}{2} = \frac{3k_F^2 + Bo}{Bo\Gamma} \delta k + O((\delta k)^2) + O(\beta), \quad \beta = -\Upsilon + \frac{kBo\Gamma}{2\Omega} \cos 2\theta. \tag{A 38}$$

Assuming $\theta \ll 1$ so that $\sin 2\theta/2 \approx \theta$, we can write $\cos 2\theta = 1 - 2\theta^2$ and substitute for θ from (A 38) to deduce

$$\beta = -\Upsilon + \frac{Bo\Gamma k}{2\Omega} \left(1 - \frac{2(3k_F^2 + Bo)^2 (k - k_F)^2}{\Gamma^2 Bo^2 k_F^2} \right). \tag{A 39}$$

Setting $\beta = 0$, solving for Γ_F and minimizing with respect to k yields

$$k_C \approx k_F(1 - \epsilon^2) \tag{A 40a}$$

and

$$\Gamma_F \approx \frac{2Oh_e \Omega k_F}{Bo} \left(1 - \frac{1}{2}\epsilon^2 \right) = 2\epsilon \left(1 + \frac{3k_F^2}{Bo} \right) \left(1 - \frac{1}{2}\epsilon^2 \right), \tag{A 40b}$$

$$\text{where } \epsilon = \frac{Oh_e \Omega k_F}{3k_F^2 + Bo}, \tag{A 41}$$

so that

$$\beta \approx Oh_e k_C^2 \left(\frac{\Gamma}{\Gamma_F} - 1 \right) - \frac{Oh_e}{2\epsilon^2} (1 + 2\epsilon^2)(k - k_C)^2 \tag{A 42}$$

and

$$\theta \approx -\frac{\epsilon}{2} + \frac{k - k_C}{2\epsilon k_F}. \tag{A 43}$$

The long-term behaviour of $H(k,\tau)$ is thus given by

$$H(k,\tau) \approx A(k)\mathrm{e}^{\beta(k)\tau}\cos\left(\frac{\Omega}{2}\tau - \frac{\epsilon}{2} + \frac{k-k_C}{2\epsilon k_F}\right). \tag{A 44}$$

In order to simplify the subsequent formulae, we introduce the decay time τ_D by writing

$$\beta(k) = (\Gamma/\Gamma_F - 1)\frac{1}{\tau_D} - \beta_1(k-k_C)^2. \tag{A 45}$$

By comparison with (A 42) we have

$$\tau_D \approx (Oh_e k_C^2)^{-1}, \quad \beta_1 \approx \frac{Oh_e}{2\epsilon^2}(1+2\epsilon^2). \tag{A 46}$$

We henceforth assume that $\Gamma < \Gamma_F$, so $\beta(k) < 0$. When $\beta_1\tau k_C^2 \gg 1$, $\beta(k)$ has a sharp maximum at k_C and we can use Laplace's method:

$$\begin{aligned} h(r,\tau) &= \int_0^\infty H(k,\tau)\mathrm{J}_0(kr)k\,\mathrm{d}k \\ &\approx \cos\frac{\Omega\tau}{2}\exp\left\{\left(\frac{\Gamma}{\Gamma_F}-1\right)\frac{\tau}{\tau_D}\right\}\int_0^\infty A(k)\mathrm{e}^{-\beta_1\tau(k-k_C)^2}\cos\frac{k-k_C}{2\epsilon k_F}\mathrm{J}_0(kr)k\,\mathrm{d}k \\ &\approx \cos\frac{\Omega\tau}{2}A(k_C)\frac{\exp\{(\Gamma/\Gamma_F-1)\tau/\tau_D\}}{\exp\{1/16\epsilon^2k_F^2\beta_1\tau\}}\sqrt{\frac{\pi}{\beta_1\tau}}\,\mathrm{J}_0(k_Cr)k_C\left[1+O\left(\frac{r^2}{4\beta_1\tau}\right)\right]. \end{aligned} \tag{A 47}$$

Here we have used the identity $\int_0^\infty \exp(-ax^2)\cos bx\,\mathrm{d}x = \exp(-b^2/4a)\sqrt{\pi/a}$. Therefore, within a certain radius $r(\tau) \sim \sqrt{\beta_1\tau}$, the surface height can be approximated by a standing wave with a radial profile prescribed by a Bessel function. We assume that the drop is within this radius as measured from all the previous impacts for which the corresponding standing wave has not yet decayed sufficiently to be negligible. This condition sets an upper bound on the allowable horizontal speed $|\mathrm{d}x/\mathrm{d}\tau|^2 < 2\beta_1(1-\Gamma/\Gamma_F)/\tau_D$. In order to approximate the wave amplitude $A(k_C)$, we use $\bar{H}(\tau) \approx \cos(\Omega\tau/2)$ in (A 33) to obtain

$$G_1(u) \approx -\frac{2}{\Omega}\sin\frac{\Omega u}{2}. \tag{A 48}$$

Substitution of (A 48) into (A 33) and (A 47) yields

$$h(r,\tau) \approx \frac{4k_C^2}{3\Omega}\sqrt{\frac{\pi}{\beta_1\tau}}\cos\frac{\Omega\tau}{2}\left[\int F(u)\sin\frac{\Omega u}{2}\,\mathrm{d}u\right]\frac{\exp\{(\Gamma/\Gamma_F-1)\tau/\tau_D\}}{\exp\{1/16\epsilon^2k_F^2\beta_1\tau\}}\mathrm{J}_0(k_Cr). \tag{A 49}$$

When $16\epsilon^2k_F^2\beta_1\tau \gg 1$, $\exp\{1/16\epsilon^2k_F^2\beta_1\tau\} \approx 1$ and by using (A 46) we can approximate (A 49) as

$$\begin{aligned} h(r,\tau) &\approx A\cos\frac{\Omega\tau}{2}\exp\{(\Gamma/\Gamma_F-1)\tau/\tau_D\}\tau^{-1/2}\mathrm{J}_0(k_Cr), \\ \text{where } A &= \frac{4\sqrt{2\pi}}{3}\frac{k_C^2k_FOh_e^{1/2}}{3k_F^2+Bo}\left[\int F(u)\sin\frac{\Omega u}{2}\,\mathrm{d}u\right]. \end{aligned} \tag{A 50}$$

The approximation (A 50) is valid when $16\epsilon^2\beta_1\tau k_F^2 \gg 1$ and $\beta_1\tau k_F^2 \gg 1$. We are interested in the bath distortion only insofar as it affects the drop dynamics; therefore, the earliest time after the initial disturbance at which we need to use

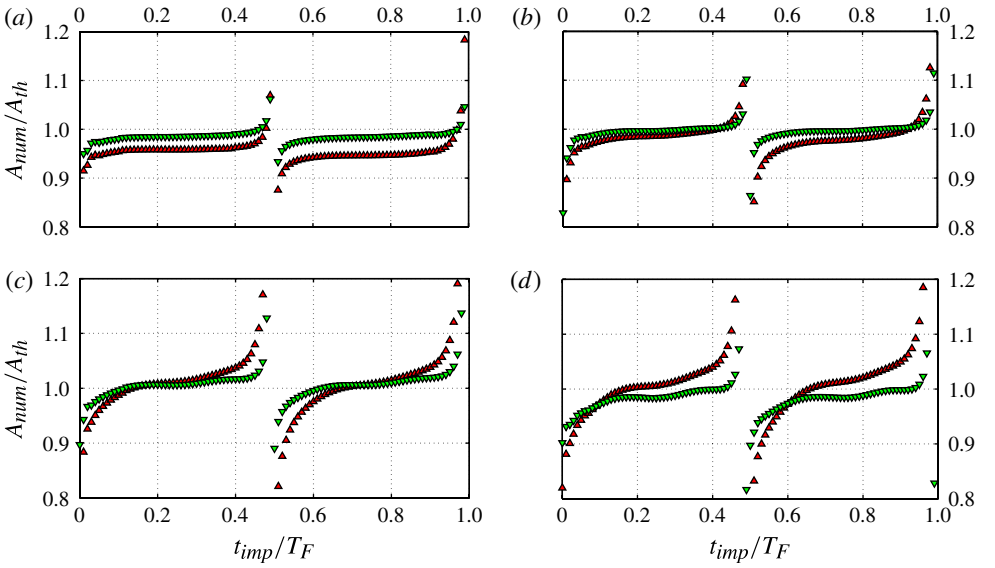

FIGURE 18. (Colour online) Comparison between the full numerical model and the long-term approximation (A 52). The bath surface is forced at time $t = t_{imp}$ and then evolved freely, and the amplitude of the standing wave $A(t) = h(0, t)$ is recorded, as computed by a full numerical scheme solving (A 27) (A_{num}) and as given by (A 52) (A_{th}). The average ratio A_{num}/A_{th} over $T_F \leqslant t \leqslant 6T_F$ (▲) and over $T_F \leqslant t \leqslant 10T_F$ (▼) is shown as a function of t_{imp}, for different combinations of oil viscosity and driving frequency: (*a*) $\nu = 10$ cSt and $f = 100$ Hz; (*b*) $\nu = 20$ cSt and $f = 80$ Hz; (*c*) $\nu = 50$ cSt and $f = 50$ Hz; and (*d*) $\nu = 100$ cSt and $f = 40$ Hz. The ratio tends to 1 for large times, except near $t_{imp} \approx (n/2)T_F$, when $G_1(t_{imp}) \approx 0$ and other wavenumbers contribute to the overall amplitude beside the region near k_F.

the approximation is on the next impact, a Faraday period later (assuming the drop is in the $(2, 1)^2$ mode). We thus require that $16\epsilon^2\beta_1\tau_F k_F^2 \gg 1$ and $\beta_1\tau_F k_F^2 \gg 1$. Employing the lower bound $k_F > (\Omega/2)^{2/3}$ following from the definition of k_F (A 26), together with (A 46), the two conditions are met provided

$$0.014 \approx (2\pi^{1/3})^{-4} \ll \left(\frac{\mu^3 f}{\rho\sigma^2}\right)^{1/3} \ll \frac{9}{8}\pi^{2/3} \approx 2.4. \tag{A 51}$$

For $\nu = 20$ cSt and 50 Hz $\leqslant f \leqslant$ 100 Hz, we obtain values between 0.09 and 0.12; while for $\nu = 50$ cSt and 40 Hz $\leqslant f \leqslant$ 80 Hz, we obtain values between 0.22 and 0.28. For lower viscosities, the lower bound is violated, while for higher viscosities, the upper bound is violated. In those cases, the approximation (A 50) becomes accurate only after multiple Faraday periods have elapsed since impact and higher-order terms in the Laplace approximation (A 47) need to be included to achieve sufficient accuracy for all drop impacts. Nevertheless, for our purposes, the leading-order approximation (A 50) will suffice.

A.5. *Numerical simulation*

The approximations to the critical wavenumber k_C, Faraday threshold Γ_F and the decay time τ_D, given by the formulae (A 40), (A 41) and (A 46), respectively, are only valid in the limit $\epsilon \ll 1$, where $\epsilon = Oh_e\Omega k_F/(3k_F^2 + Bo)$. As the values of these parameters play a crucial role in the evolution of the standing waves near the Faraday threshold,

ν (cSt)	f (Hz)	ϵ	Γ_F		k_C/k_F		τ_F/τ_D		$\beta_1 k_F^2 \tau_F$	
			Theor.	Num.	Theor.	Num.	Theor.	Num.	Theor.	Num.
10	100	0.097	3.324	3.326	0.991	0.988	0.804	0.816	44.35	44.69
10	120	0.102	4.526	4.530	0.990	0.987	0.868	0.883	43.07	43.41
20	60	0.156	2.562	2.566	0.976	0.971	1.126	1.173	25.60	26.26
20	80	0.170	4.220	4.228	0.971	0.965	1.303	1.369	25.32	25.99
20	90	0.176	5.159	5.170	0.969	0.962	1.373	1.447	25.08	25.76
50	40	0.311	2.707	2.731	0.903	0.904	1.664	1.967	12.59	14.38
50	50	0.335	4.028	4.073	0.888	0.888	1.893	2.311	13.12	15.03
50	60	0.353	5.514	5.586	0.875	0.874	2.056	2.577	13.45	15.47
100	40	0.563	4.334	4.646	0.683	0.772	1.721	3.295	9.51	13.47
100	50	0.597	6.251	6.789	0.644	0.746	1.775	3.779	10.29	14.65

TABLE 4. Comparison of some of the critical parameters describing the standing-wave evolution, as calculated numerically and given by the theoretical approximations (A 40) and (A 46), for the combinations of oil viscosity ν and driving frequency f at which walking occurs. These are the Faraday threshold $\Gamma_F = \gamma_F/g$, the ratio of the most unstable wavenumber k_C to the Faraday wavenumber k_F, the ratio of the Faraday period τ_F to the decay time τ_D, and the parameter $\beta_1 k_F^2 \tau_F$, which describes the increase of the decay rate of $H(k)$ as k moves away from k_C. The parameter ϵ, defined in (A 41), was assumed small in our theoretical analysis. We observe a good match for small ν, which gradually worsens as ν (and thus also ϵ) increases. The error is of the order of ϵ^2.

in order to achieve a better match with experiments for larger values of ϵ (e.g. when $\nu = 50$ cSt), we calculate them numerically. Starting from the recurrence relation (A 35), the conditions $\hat{H}_n = \hat{H}^*_{-n}$ and $\lim_{n\to\infty} |n\hat{H}_n| = 0$ yield a unique solution for Γ, given β. The solution can be found by choosing arbitrary values of $\hat{H}_N$ and $\hat{H}_{N-2}$ for some large odd N, then working backwards using the recurrence relation and finally rescaling all terms in order to satisfy the reality condition $\hat{H}_n = \hat{H}^*_{-n}$. Choosing $N > 15$ usually suffices to achieve 10-digit accuracy in Γ. Thus, given k and β, we can find the corresponding Γ. Setting $\beta = 0$ gives us $\Gamma_F(k)$, and minimizing with respect to k yields k_C and Γ_F. In order to obtain τ_D, we need only calculate Γ' corresponding to some small β and then use the relation $\tau_D = (\Gamma'/\Gamma_F - 1)/\beta$. Table 4 compares the values obtained analytically and numerically.

In our analytic treatment of the standing-wave evolution, we have approximated the time-periodic part $\bar{H}(\tau) = \sum_{-\infty}^{\infty} \hat{H}_n \exp(\mathrm{i}\Omega n\tau/2)$ of the Hankel transform of the surface height by its first Fourier component: $\bar{H}(\tau) \approx \sum_{-1}^{1} \hat{H}_n \exp(\mathrm{i}\Omega n\tau/2) = \cos((\Omega\tau/2) + \theta)$ ($\hat{H}_{2m} = 0$ for the sub-harmonic mode). When the viscosity is appreciable, accurate representation of the time periodicity requires inclusion of the next Fourier modes $\hat{H}_{\pm 3}$. Therefore, the approximation to the standing-wave evolution, which will be used in the numerical model, is given by (compare with (A 50)):

$$h(r,\tau) \approx \frac{4\sqrt{2\pi}}{3} \frac{k_C^2 k_F Oh_e^{1/2}}{3k_F^2 + Bo} \left[\int F(u) G_1(u)\, \mathrm{d}u \right] \times \frac{\bar{H}(\tau)}{\sqrt{\tau}} \exp\left\{ (\Gamma/\Gamma_F - 1) \frac{\tau}{\tau_D} \right\} \mathrm{J}_0(k_C r), \tag{A 52}$$

where

$$\bar{H}(\tau) = \sum_{n=-2}^{1} \hat{H}_{2n+1} \exp\{\mathrm{i}\Omega(n+1/2)\tau\} \tag{A 53}$$

and $G_1(u)$ is given by (A 33) with $\beta = 0$. The values of $\hat{H}_{2n+1}$ are obtained by solving the recurrence relation (A 35) with $\beta = 0$, $k = k_C$ and subject to the conditions $\hat{H}_n = \hat{H}^*_{-n}$, $\lim_{|n|\to\infty} |n\hat{H}_n| = 0$ and $|\hat{H}_1| = 1$. We illustrate the accuracy of the approximation (A 52) in figure 6, where it is compared to a full numerical simulation of the bath deformation. The full numerical solution was obtained by solving (A 27) for $k_n = n\delta k$ with $\delta k = 0.001$ and $1 \leqslant n \leqslant 2000$ and approximating $h(r,t) \approx \sum_{n=1}^{2000} H(k_n,\tau)\mathrm{J}_0(k_n r)k_n\delta k$. We observe a good match between the full numerical solution and the approximation (A 52) for both viscosities.

REFERENCES

BENJAMIN, T. & URSELL, F. 1954 The stability of the plane free surface of a liquid in vertical periodic motion. *Proc. R. Soc. Lond.* A **225**, 505–515.

DE BROGLIE, L. 1987 Interpretation of quantum mechanics by the double solution theory. *Ann. Fond. Louis de Broglie* **12**, 1–23 (English translation).

BUSH, J. W. M. 2010 Quantum mechanics writ large. *Proc. Natl Acad. Sci.* **107**, 17 455–17 456.

CHANG, E. J. & MAXEY, M. R. 1994 Unsteady flow about a sphere at low to moderate Reynolds number. Part 1. Oscillatory motion. *J. Fluid Mech.* **277**, 347–379.

COUDER, Y. & FORT, E. 2006 Single-particle diffraction and interference at macroscopic scale. *Phys. Rev. Lett.* **97**, 154101.

COUDER, Y., FORT, E., GAUTIER, C. H. & BOUDAOUD, A. 2005*a* From bouncing to floating: noncoalescence of drops on a fluid bath. *Phys. Rev. Lett.* **94**, 177801.

COUDER, Y., PROTIÈRE, S., FORT, E. & BOUDAOUD, A. 2005*b* Walking and orbiting droplets. *Nature* **437**, 208.

EDDI, A., FORT, E., MOISY, F. & COUDER, Y. 2009 Unpredictable tunneling of a classical wave-particle association. *Phys. Rev. Lett.* **102**, 240401.

EDDI, A., MOUKHTAR, J., PERRARD, S., FORT, E. & COUDER, Y. 2012 Level splitting at macroscopic scale. *Phys. Rev. Lett.* **108**, 264503.

EDDI, A., SULTAN, E., MOUKHTAR, J., FORT, E., ROSSI, M. & COUDER, Y. 2011 Information stored in Faraday waves: the origin of a path memory. *J. Fluid Mech.* **674**, 433–463.

EDDI, A., TERWAGNE, D., FORT, E. & COUDER, Y. 2008 Wave propelled ratchets and drifting rafts. *Europhys. Lett.* **82**, 44001.

FLÜGGE, S. 1959 *Handbuch der Physik: Strömungsmechanik I.* Springer.

FORT, E., EDDI, A., BOUDAOUD, A., MOUKHTAR, J. & COUDER, Y. 2010 Path-memory induced quantization of classical orbits. *Proc. Natl Acad. Sci.* **107**, 17 515–17 520.

GILET, T. & BUSH, J. W. M. 2009 The fluid trampoline: droplets bouncing on a soap film. *J. Fluid Mech.* **625**, 167–203.

GOLDMAN, A. J., COX, R. G. & BRENNER, H. 1967 Slow viscous motion of a sphere parallel to a plane wall – I: Motion through a quiescent fluid. *Chem. Engng Sci.* **22**, 637–651.

HARRIS, D. M., MOUKHTAR, J., FORT, E., COUDER, Y. & BUSH, J. W. M. 2013 Wave-like statistics from pilot-wave dynamics in a circular corral. *Phys Rev.* E (submitted).

HARTLAND, S. 1971 The pressure distribution in axisymmetric draining films. *J. Colloid Interface Sci.* **35**, 227–237.

KUMAR, K. 1996 Linear theory of Faraday instability in viscous liquids. *Proc. Math. Phys. Engng Sci.* **452**, 1113–1126.

LAMB, H. 1932 *Hydrodynamics*. Cambridge University Press.

MOLÁČEK, J. & BUSH, J. W. M. 2012 A quasi-static model of drop impact. *Phys. Fluids* **24**, 127103.

MOLÁČEK, J. & BUSH, J. W. M. 2013 Drops bouncing on a vibrating bath. *J. Fluid Mech.* **727**, 582–611.

OZA, A. U., ROSALES, R. R. & BUSH, J. W. M. 2013 A trajectory equation for walking droplets: hydrodynamic pilot-wave theory. *J. Fluid Mech.* (submitted).

PROSPERETTI, A. 1976 Viscous effects on small-amplitude surface waves. *Phys. Fluids* **19**, 195–203.

PROTIÈRE, S., BOUDAOUD, A. & COUDER, Y. 2006 Particle-wave association on a fluid interface. *J. Fluid Mech.* **554**, 85–108.

PROTIÈRE, S., COUDER, Y., FORT, E. & BOUDAOUD, A. 2005 The self-organization of capillary wave sources. *J. Phys.: Condens. Matter* **17**, S3529–S3535.

SHIROKOFF, D. 2013 Bouncing droplets on a billiard table. *Chaos* **23**, 013115.

TORBY, B. J. 1984 *Advanced Dynamics for Engineers*. Holt, Rinehart and Winston.

WALKER, J. 1978 Drops of liquid can be made to float on the liquid. What enables them to do so? *The Amateur Scientist, Sci. Am.* **238**, 151–158.

WIND-WILLASSEN, Ø., MOLÁČEK, J., HARRIS, D. M. & BUSH, J. W. M 2013 Exotic states of bouncing and walking droplets. *Phys. Fluids* (submitted).